PHYSICAL REVIEW D **111,** 123034 (2025)

Probing fermionic asymmetric dark matter cores using global neutron star properties

Nathan Rutherford,[1,*] Chanda Prescod-Weinstein,[1,†] and Anna Watts[2,‡]

[1]*Department of Physics and Astronomy, University of New Hampshire,*
Durham, New Hampshire 03824, USA
[2]*Anton Pannekoek Institute for Astronomy, University of Amsterdam,*
Science Park 904, 1098XH Amsterdam, The Netherlands

(Received 3 October 2024; accepted 8 May 2025; published 23 June 2025)

It is possible for asymmetric dark matter (ADM) to accumulate in neutron star interiors and affect their global properties. Considering the effects of this accumulation, neutron star mass-radius measurements can deliver new insights into the cold dense matter equation of state (EoS). In this paper, we employ Bayesian parameter estimation using real and synthetic neutron star mass-radius data to infer constraints on the combined baryonic matter and fermionic ADM EoS, where the fermionic ADM forms a core in the neutron star interior. Using currently available mass-radius data, we find that the lower bound of the ratio between the ADM effective self-repulsion strength (g_χ/m_ϕ) and particle mass (m_χ) can be constrained at the 68% (95%) credible level to $10^{-6.59}$ ($10^{-7.77}$). We also find that, if neutron star mass-radius measurement uncertainties are reduced to the 2% level, the constraints on the lower bound of the ratio of g_χ/m_ϕ to m_χ can be improved to $10^{-6.49}$ and $10^{-7.68}$ at the 68% and 95% credible levels, respectively. However, all other combinations, of m_χ, g_χ, and the ADM mass-fraction, F_χ (i.e., the ratio of the gravitational ADM mass to the gravitational mass of the neutron star), are unconstrained. Furthermore, in the pressure-energy density and mass-radius planes, the inferences which include the possibility of fermionic ADM cores are nearly identical with the inferences that neglect fermionic ADM for $F_\chi \leq 1.7\%$ and neutron star mass-radius uncertainties $\geq 2\%$. Therefore, we find that neutron star mass-radius measurements can constrain the ratio of g_χ/m_ϕ to m_χ. Moreover, since the pressure-energy density and mass-radius posteriors which include fermionic ADM overlap with those that neglect fermionic ADM, we find that neutron stars with ADM are indistinguishable from purely baryonic stars. This implies that neutron stars with ADM are equally as consistent with the available mass-radius data as neutron stars without ADM.

DOI: 10.1103/PhysRevD.111.123034

I. INTRODUCTION

The extremely compact nature of neutron stars provides a unique environment to probe the behavior of matter at supranuclear densities. Theoretical models of neutron star interiors predict many different types of baryonic matter, such as neutron-rich matter, nuclear pasta, hyperons, and deconfined quarks [1–7]. The microphysics of these hypothetical forms of matter are encoded by the equation of state (EoS), which describes the relation between the pressure and energy density maintained throughout the star. The dense matter EoS can be determined from knowing the gravitational masses and radii of neutron stars. In particular, each EoS can be mapped to a unique mass-radius relation, i.e., the numerical expression that relates all possible, stable neutron star mass and radii, through the Tolman-Oppenheimer-Volkoff (TOV) equations [8]. Thus, measurements of neutron stars can be used to characterize the mass-radius curve, and thus constrain each hypothetical dense matter EoS.

Analyzing the x-ray pulse profile (a rotationally phase and energy-resolved x-ray count spectrum) can be used to infer the masses and radii of neutron stars through the pulse profile modeling (PPM) technique. PPM is a relativistic ray-tracing technique that can be used to extract valuable information encoded in the pulse profile, such as mass, radius, and hot spot geometry (for more details on PPM see [9–11]). So far, data from NASA's Neutron Star Interior Composition Explorer (NICER) [12], informed where possible by mass priors from pulsar timing, has been used to infer the masses and radii of three millisecond pulsars using the PPM technique: PSR J0740 + 6620 [13–18], PSR J0030 + 0451 [19–21], and most recently, PSR J0437 − 4715 [22,23]. Constraints have also been placed on a fourth millisecond pulsar, PSR J1231-1411, but these constraints are weaker than the others and will

---

[*] Contact author: nathan.rutherford@unh.edu
[†] Contact author: chanda.prescod-weinstein@unh.edu
[‡] Contact author: A.L.Watts@uva.nl

therefore be neglected in this work [24]. The mass-radius measurements of these pulsars have been used in many analyses to set constraints on the dense matter EoS (see e.g., [15,20,25–35]). Most recently, [34] has shown that the inferences with the newest mass-radius results from NICER improve the reliability of our understanding on the neutron star EoS via the updated chiral effective field theory (χEFT) calculations of [36] and the degree in which the results are data driven. However, the uncertainty of the cold dense matter EoS remains.

In the near future, improved mass-radius constraints on targets already analyzed by NICER are expected. Additionally, the mass-radius measurements of four more sources are anticipated. During the next decade, large-area x-ray spectral-timing missions are anticipated to perform PPM on more neutron stars with improved uncertainties. Such missions include the Chinese enhanced X-ray Timing and Polarimetry mission concept [37], the NASA probe-class Spectroscopic Time-Resolving Observatory for Broadband Energy X-rays (STROBE-X) mission concept [38], and the European Space Agency's L-class Advanced Telescope for High ENergy Astrophysics mission [39].

Currently, many of the EoS studies that consider PPM-derived mass-radius measurements only account for the presence of baryonic matter and its potential phase transitions. However, there is a growing understanding that dark matter may form part of neutron star structures and therefore affect the observable properties of neutron stars. To fully assess the range of neutron star EoSs, we must therefore also study the inclusion of a dark matter component in our models. Dark matter can occupy two spatial regimes: a dark matter halo that extends through and beyond the baryonic radius of the neutron star, and a dark matter core inside the neutron star's interior. Dark matter halos around neutron stars have been shown to increase the gravitational masses and tidal deformabilities of the stars when compared to a neutron star with no asymmetric dark matter (ADM) with an identical central baryonic energy density, if the dark matter mass distribution is mostly beyond the baryonic surface [40–46]. However, if most of the dark matter halo distribution resides within the baryonic radii of neutron stars, halos can reduce the gravitational masses and radii of these stars (see e.g., [47]). In addition, the presence of any dark matter halo can significantly impact the exterior space-time around neutron stars, which would alter the interpretation of NICER's mass-radius measurements [47–49]. Interestingly, dark matter halos could possibly form stable ultracompact neutron stars with compactness greater than $1/3$, which could serve as a black hole mimicker [50]. If dark matter forms a core inside neutron star interiors, the gravitational masses, radii, and tidal deformabilities have been shown to decrease when compared to their purely baryonic counterparts with the same central baryonic energy density [51–58]. Therefore, it is evident that, because dark matter can affect the measurable properties of neutron stars, the possible presence of it must be accounted for in analyses of the neutron star mass-radius measurements and the EoS.

There are a variety of proposed methods to constrain the presence of dark matter in and around neutron stars. For instance, by considering one or multiple representative baryonic EoSs, constraints on the dark matter particle mass, mediator mass, and mass-fraction can be made using gravitational wave and neutron star mass-radius measurements [45,48,54,55,59–74]. More specifically, using one or more baryonic EoSs allows for constraints on the dark matter mass-fraction as a function of particle mass [45,54,55,63,64], the dark matter Fermi momentum and particle mass [59,73], several dark matter parameters by imposing hard cutoffs on the maximum neutron star mass and tidal deformability of a $1.4M_{\odot}$ neutron star [61,62,69–71,74], correlations between dark matter and baryonic matter parameters [65–68,72], and Bayesian inferences to estimate the dark matter parameter space [48,60]. Analytical calculations of the maximum accumulated dark matter mass before gravitational collapse to a black hole inside a neutron star can be used to tightly constrain dark matter models through observations of old neutron stars [75–78]. When an additional dark matter component is considered in simulations of binary neutron star mergers it has been shown that dark matter can leave detectable signatures on the gravitational wave and electromagnetic counterparts, which can constrain the dark matter particle mass and the total accumulated dark matter mass [79–81]. Finally, due to their extremely compact natures, neutron stars can efficiently capture dark matter within their interiors and thus can provide constraints on the dark matter–nucleon cross section and particle mass [82].

In our previous work [83], we investigated constraints on bosonic ADM cores inside neutron stars by performing a full Bayesian inference in which all parameters in the neutron star EoS model are allowed to vary. We assumed the dark matter was 100% comprised of the self-repulsive bosonic ADM of [40]. The main motivation of the ADM paradigm suggests that the cosmic history between dark matter and baryonic matter is strongly tied together given that the observed dark matter mass density in the Universe is only 5 times greater than that of baryonic matter. That is, similar to the baryon asymmetry in the early Universe, dark matter also had an asymmetry between it and anti–dark matter, which produced the relic abundance of dark matter observed today in the Universe [84,85]. A "dark asymmetry" between dark matter and anti–dark matter in the early Universe would allow for small attractive interactions with baryonic matter and substantial repulsive self-interactions.

By combining the EoS of the [40] bosonic ADM model with the parametrized piecewise polytropic (PP) model of [1] and restricting the study to simulated neutron star mass-radius measurements with and without bosonic ADM cores, in [83] we explored the possible inferred constraints on both the bosonic ADM and baryonic EoSs. From these inferences, we found that the uncertainties on the baryonic EoS are relaxed when bosonic ADM cores are taken into account. Moreover, in [83] we found that, if the baryonic EoS could be constrained more tightly, constraints on the ADM mass-fraction and the ratio of the effective bosonic ADM self-repulsion strength to the particle mass can be made. Last, we concluded that the ADM particle mass and self-repulsion cannot be individually constrained using neutron star mass-radius measurements.

Several studies, that have also studied dark matter admixed neutron stars using NICER mass-radius measurements and/or gravitational wave measurements from LIGO/VIRGO are [45,48,49]. In [48], the authors studied the impact of dark matter halos on the pulse profile of neutron stars and performed a Bayesian analysis on the [40] fermionic ADM model with a fixed baryonic matter EoS. Additionally, they restricted their analysis to dark matter cores and diffuse halos. Their inference is based on the posterior distributions of two NICER pulsars, namely PSR $\mathrm{J}0740+6620$ and PSR $\mathrm{J}0030+0451$. Although [48] did not determine constraints on the ADM self-repulsion strength and mass-fraction, they did infer constraints on the fermionic ADM particle mass. In particular, they determined the ADM particle mass is favored to be less than 1.5 GeV for halos and ADM cores favor masses near 0.6 GeV. In [49], the authors also studied the affect of dark matter halos on the pulse profile of neutron stars and studied the constraints on bosonic dark matter using two baryonic EoS models with different stiffness. Moreover, [49] performed a scan over the bosonic dark matter particle mass, self-interaction strength, and mass-fraction using both baryonic matter EoS models and compared the results to the 95% confidence intervals of the NICER and LIGO/VIRGO measurements. Here, they found that the maximum allowed dark matter mass-fraction is around 5% and 20% for the relatively soft and stiff baryonic EoSs, respectively. In addition, [49] also found that the allowed region of particle masses and self-repulsion strengths shrinks for increasing mass-fraction for both baryonic EoSs. Last, in [45], the authors considered ten baryonic EoS models of varying stuffiness and a fermionic dark matter model with repulsive and attractive self-interactions. Their analysis consisted of comparing various fermionic dark matter configurations using the 95% contours of the NICER and LIGO/VIRGO measurements as hard cutoffs to rule one configuration in or out. Here, [45] found that dark matter particle masses in the range of [0.1, 30] GeV with Fermi momenta in the interval [0.01, 0.07] GeV can match the data contours. In order to constrain dark matter in neutron stars, all three studies used at most a handful of baryonic EoSs and used NICER and/or LIGO/VIRGO measurements.

In this work, we take a different approach to those found in the literature and expand on our prior work in [83] by taking into account fermionic ADM cores, considering realistic ADM accumulation mechanisms that apply to all physically allowed ADM particle masses, and including both real and synthetic PPM-derived mass-radius data. Modeling the dark matter core as fermionic ADM instead of bosonic ADM is physically interesting because fermionic ADM cores have additional support against gravity through the Fermi degeneracy pressure, thus expanding the allowed ADM parameter space to be studied because the self-repulsion is allowed to be zero. We additionally consider real neutron star mass-radius data for this work because [58] showed that the presence of ADM cores does not modify the universal relations used to model the oblateness of neutron stars.[1] By considering both real and synthetic data in addition to ADM accumulation mechanisms that apply to the entire physically allowed parameter space, this work will be able to investigate current and potential future constraints on fermionic ADM cores.

In this work, we assume the fermionic ADM cores are described by the [40] model and neglect the possibility of ADM halo configurations, because the existence of any halo will alter the exterior space-time and thus modify how PPM is performed. This work considers the mass-radius measurements of PSR $\mathrm{J}0740+6620$ [14] and PSR $\mathrm{J}0030+0451$ [19]. There have been several updates to PSR $\mathrm{J}0740+6620$ [16,17] and PSR $\mathrm{J}0030+0451$ [21], as well as a new mass-radius measurement for PSR $\mathrm{J}0437-4715$ [22], which was released during the completion of this work. However, we still consider the mass-radius posteriors of PSR $\mathrm{J}0030+0451$ [19] and PSR $\mathrm{J}0740+6620$ [14] for two key reasons: the first is so that this work is fully comparable to our previous work on bosonic ADM [83] and the other is because our synthetic scenario best demonstrates what can be achieved with tighter mass-radius uncertainties.

For the simulated neutron star data, we consider six possible STROBE-X sources because the STROBE-X mission is expected to provide lower uncertainties than NICER [38,88]. We call this scenario, *Future-X*, after the original *Future-X* scenario in our previous work. By incorporating fermionic ADM with both real and synthetic data into our Bayesian framework, this work aims to quantify the possible constraints on the fermionic ADM EoS for current missions and future missions, namely NICER and STROBE-X. Furthermore, the other objective is to determine the effects of including fermionic ADM on the neutron star pressure–energy density and mass-radius posteriors.

The work presented in this manuscript shows that the current NICER and future STROBE-X measurements are able to place constraints on the lower bound of the ratio between the ADM particle mass and effective self-repulsion strength. However, under the current uncertainties of the baryonic EoS, neither NICER nor STROBE-X can constrain the fermionic ADM particle mass, effective self-repulsion strength, or mass-fraction. Finally, we find that the mass-radius ADM admixed neutron star posteriors are equally as consistent with the data as the counterparts that neglect ADM, which implies that NICER and STROBE-X cannot distinguish between the two cases.

---

[1] For further details on the universal oblateness relations of neutron stars see [86,87].

This paper is organized as follows. In Sec. II, we motivate the two-fluid TOV equations and describe the baryonic matter and fermionic ADM EoSs. Section III discusses our Bayesian inference framework for providing constraints on the ADM admixed neutron star EoS, the baryonic matter EoS priors, the constraints on the fermionic ADM EoS parameter space, and the selected neutron star mass-radius measurements. In Sec. IV, we study the inferences for both the NICER data and *Future-X* scenario. Finally, in Sec. V, we discuss our results. Throughout this work, we use the metric signature $\mathrm{diag}(-,+,+,+)$.

II. MODELING THE STRUCTURE OF ADM ADMIXED NEUTRON STARS

Traditionally, the mass-radius relation of neutron stars is computed by iteratively solving the TOV equations [89,90] for a given baryonic matter EoS and range of central energy densities [8]. However, to compute the mass-radius relation of neutron stars with ADM, the single fluid mass-radius relation calculation must be modified. In this section, we describe how to model the structure of ADM admixed neutron stars using the two-fluid formalism, and describe the baryonic matter and ADM EoSs used in our analysis. The combination of the baryonic matter EoS, ADM EoS, and two-fluid formalism, allow for the ADM admixed neutron star mass-radius relation to be computed.

A. The two-fluid formalism

The global properties, such as mass and radius, of an ADM admixed neutron star can be computed by adopting the two-fluid formalism, which assumes that the interactions between the Standard Model and ADM are solely gravitational (see e.g., [47,49,51,55,58,63,80,91,92]). The two-fluid formalism is an appropriate framework to study ADM admixed neutron stars because any nongravitational interfluid interaction between ADM and the Standard Model is expected to be negligible [93,94].[2] The assumption that ADM and baryonic matter interact only gravitationally implies that ADM and baryonic matter satisfy their own conservation of the energy-momentum equation. Thus, both ADM and baryonic matter can be treated as two distinct fluids, which can be expressed in terms of pressure and energy density as

$$p(r) = p_B(r) + p_\chi(r), \tag{1}$$

$$\varepsilon(r) = \varepsilon_B(r) + \varepsilon_\chi(r), \tag{2}$$

where p_B (ε_B) is the baryonic matter pressure (energy density) as a function of radius r and p_χ (ε_χ) is the ADM pressure (energy density) as function of r. The substitution of Eqs. (1) and (2) into the single-fluid TOV equations yields the two-fluid TOV equations:

$$\frac{dp_B}{dr} = -(\varepsilon_B + p_B)\frac{Gc^2M(r) + 4\pi r^3 G p(r)}{c^2 r[rc^2 - 2GM(r)]}, \tag{3}$$

$$\frac{dp_\chi}{dr} = -(\varepsilon_\chi + p_\chi)\frac{Gc^2M(r) + 4\pi r^3 G p(r)}{c^2 r[rc^2 - 2GM(r)]}, \tag{4}$$

$$\frac{dM_B(r)}{dr} = 4\pi r^2 \frac{\varepsilon_B(r)}{c^2}, \tag{5}$$

$$\frac{dM_\chi(r)}{dr} = 4\pi r^2 \frac{\varepsilon_\chi(r)}{c^2}, \tag{6}$$

where $M_\chi(r)$ is the gravitational mass of ADM, $M_B(r)$ is the gravitational mass of baryonic matter, and $M(r) = M_B(r) + M_\chi(r)$. The two-fluid TOV equations can then be simultaneously solved for the gravitational masses, radii, and pressures of each fluid given their respective EoSs and central energy densities. More specifically, the pressures and gravitational masses of ADM and baryonic matter are solved simultaneously until either one of the fluid pressures reaches zero. The integration is stopped and then resumed using the single-fluid TOV equations with the last pressure value of the remaining fluid as the initial condition. Since the two-fluid TOV equations can be solved to obtain the gravitational masses and radii of both ADM and baryonic matter, they can also be used to numerically compute the ADM admixed mass-radius relation. Similar to how the baryonic matter neutron star mass-radius relation is numerically computed, the ADM admixed neutron star mass-radius relation is obtained by iteratively solving the two-fluid TOV equations for a given EoS and range of central energy densities for both ADM and baryonic matter, respectively.

The two-fluid TOV equations allow for a clear distinction between the ADM core radius (R_χ) and the baryonic matter radius (R_B), which makes it possible to define the ADM mass-fraction, F_χ. The mass-fraction is defined as the ratio of the ADM gravitational mass to the total gravitational mass of the ADM admixed neutron star, and it is given by

$$F_\chi = \frac{M_\chi(R_\chi)}{M_\chi(R_\chi) + M_B(R_B)}, \tag{7}$$

---

[2] We would like to note that the choice of using the two-fluid formalism is not entirely consistent with the ADM paradigm because it neglects any interaction of dark matter with baryonic matter, which is necessary to generate the dark asymmetry between ADM and anti-ADM. However, since this work assumes that the coupling of baryonic matter to ADM is small compared to the coupling strength of ADM to itself (see Sec. II B for further details) and that the dominant interaction between ADM and baryonic matter is gravitational, the two-fluid formalism is a well-motivated treatment to study ADM inside neutron stars. Additionally, since this work considers the [1] parametrized PP model for the baryonic EoS, the Standard Model baryon current cannot be computed because there is no associated Lagrangian with the model. Although capturing the uncertainties of the baryonic EoS and the interaction term of baryonic matter with ADM in the ADM EoS needs further work, this can be improved in the future, e.g., using the two-fluid interacting system considered in [95].

where $M_\chi(R_\chi)$ is the total accumulated ADM gravitational mass evaluated at R_χ and $M_B(R_B)$ is the baryonic matter gravitational mass evaluated at R_B. The ADM mass-fraction is useful because the total gravitational mass and radius of an ADM admixed neutron star is strongly dependent on the value of F_χ (see [54,57,96]). Moreover, when specific assumptions about the baryonic matter EoS are made, the ADM mass-fraction can be constrained tightly by neutron star measurements [54,55,83,91] and can be used to place constraints on the ADM particle mass [49,57,64,91]. The F_χ is an optimal parameter to consider in our analysis. Finally, to compute the structure of an ADM admixed neutron star for a given F_χ and central baryonic energy density, we follow the numerical algorithm outlined in [83].

B. The baryonic matter and ADM EoSs

In order to model neutron stars that have baryonic matter and potential fermionic ADM core components, we need to solve the two-fluid TOV equations. This requires an EoS for each type of matter. While it is common practice to model the baryonic matter EoS using one or more of the available tabulated EoSs [40,47,48,51–53,58,63], we model the baryonic matter EoS using the parametrized PP model used in [1,25–27,34,97]. We employ the PP model because it, as well as other polytropic models, can fit many of the tabulated EoSs [98]. Moreover, when a wide range of PP EoSs are sampled, the PP model is able to capture the uncertainties in the baryonic EoS due to its parametrized nature. This allows for the PP model to span much of the physically viable space in the mass-radius plane. The parametrized PP model is described by three varying polytropes connected at two varying transition densities and considers the calculations of χEFT at low density. In particular, for densities $\lesssim 0.5n_0$ ($n_0 = 0.16\ \mathrm{fm}^{-3}$) we consider the neutron star crust to be described by the Baym-Pethick-Sutherland crust EoS [99], which we then connect to a single polytropic fit of the χEFT band of [1] between $0.5n_0$ and $1.1n_0$. At densities above $2n_0$, the χEFT calculations grow increasingly uncertain and eventually break down [100]. Although, χEFT calculations have been considered up to 1.5–$2.0n_0$ in other EoS analyses (see e.g., [7,34,101]), we do not expect the difference in these choices to affect the inferences on the fermionic ADM EoS parameters, as the χEFT calculations only affect the uncertainties on the baryonic EoS, which is beyond the scope of this work. Additionally, this work seeks to be comparable to our previous work [83]. Thus, for densities $\geq 1.1n_0$, we connect the [1] χEFT band to the high-density piecewise polytropic parametrization. Modeling the baryonic EoS in this way allows us to simultaneously consider the tight constraints delivered by the χEFT formalism and systemically study the neutron star mass-radius plane (see [1,98,102]).

Our fermionic ADM core is that of [40], which describes an MeV–GeV mass-scale spin-$1/2$ ADM particle χ with repulsive self-interactions mediated by the exchange of an eV–MeV mass-scale vector gauge boson ϕ_μ. The ADM vector gauge boson also carries the Standard Model baryon number in order to create the asymmetry between dark matter and anti–dark matter particles in the early Universe that is needed to produce the present dark matter mass density of the Universe.

In order to obtain the fermionic ADM EoS, [40] assumed that $g_B \ll g_\chi$, where g_χ is the interacting strength between χ and ϕ_μ and g_B is the interaction strength of ϕ_μ with the Standard Model baryon current. Although robust calculations of this inequality have not been done yet, assuming that $g_B \ll g_\chi$ is physically reasonable because it is expected that $g_\chi \in [10^{-6}, 1]$ for ϕ_μ in the eV–MeV mass scale, which is at least 4 orders of magnitude greater than the $g_B \leq 10^{-10}$ constraint [40,94].[3] Therefore, in order to obey the assumption that $g_B \ll g_\chi$, we approximate the effective self-repulsion strength to a nonzero value that produces ADM cores similar to the physically allowed value of zero in the Appendix. Given the assumption that $g_B \ll g_\chi$, and by assuming that all of the possible accumulated ADM has thermally equilibrated within the neutron star then the ADM EoS can be computed in the zero-temperature limit. Thus, with $\hbar$ and c restored, the [40] fermionic ADM EoS is expressed as

$$\varepsilon_\chi = \frac{c^5 m_\chi^4}{8\pi^2\hbar^3}\left[\sqrt{1+z^2}(2z^3+z) - \ln(z+\sqrt{1+z^2})\right] + \frac{g_\chi^2}{2m_\phi^2}\frac{c^5(m_\chi z)^6}{\hbar^3(3\pi^2)^2}, \tag{8}$$

$$p_\chi = \frac{c^5 m_\chi^4}{8\pi^2\hbar^3}\left[\sqrt{1+z^2}\left(\frac{2}{3}z^3 - z\right) + \ln(z+\sqrt{1+z^2})\right] + \frac{g_\chi^2}{2m_\phi^2}\frac{c^5(m_\chi z)^6}{\hbar^3(3\pi^2)^2}, \tag{9}$$

where ε_χ is the fermionic ADM energy density, p_χ is the fermionic ADM pressure, and $z = \hbar k_\chi / m_\chi c$ is the relativity parameter defined in terms of the ADM Fermi momentum k_χ. By inserting the baryonic matter and fermionic ADM EoSs into the two-fluid TOV equation, the ADM admixed neutron star mass-radius relation can be computed.

III. METHODOLOGY

We now show how to construct our Bayesian inference framework that considers both baryonic matter and ADM inside neutron star interiors. In this section, we discuss this inference framework, the prior space of the PP

---

[3] Note that g_χ is allowed be zero in the [40] fermionic ADM model because the Fermi degeneracy pressure offers the ADM core support against gravitational collapse.

parametrization of the baryonic EoS, constraints on the fermionic ADM EoS parameters, and the source selection for both the real and synthetic data analyses.

A. Bayesian framework

We use the inference framework developed in [83], which adapts the Bayesian analysis of [25–27,34,97] to include the possible presence of an ADM EoS. In particular, we use the open source EoS inference code NEoST v2.0.0, which includes ADM functionality [103].[4] A full reproduction package, including the posterior samples and scripts to generate the plots in this work, is available in a Zenodo repository at [104].

We use Bayes' theorem to write the posterior distribution on all ADM and baryonic EoSs as

$$\begin{aligned} p(\boldsymbol{\theta},\boldsymbol{\varepsilon_c}|\mathbf{d}) &\propto p(\boldsymbol{\theta})p(\boldsymbol{\varepsilon_c}|\boldsymbol{\theta})p(\mathbf{d}|\boldsymbol{\theta},\boldsymbol{\varepsilon_c}) \\ &\propto p(\boldsymbol{\theta})p(\boldsymbol{\varepsilon_c}|\boldsymbol{\theta})p(\mathbf{d}|\mathbf{M}(\boldsymbol{\theta},\boldsymbol{\varepsilon_c}),\mathbf{R}(\boldsymbol{\theta},\boldsymbol{\varepsilon_c})), \end{aligned} \tag{10}$$

where $\boldsymbol{\theta}$ is the vector containing all ADM and baryonic EoS parameters, $\boldsymbol{\varepsilon_c}$ is the vector containing the baryonic and ADM central energy densities, $\mathbf{d}$ is the vector containing the masses and radii of the sources from each scenario, $\mathbf{M}(\boldsymbol{\theta},\boldsymbol{\varepsilon_c})$ is the mass of a produced admixed neutron star, and $\mathbf{R}(\boldsymbol{\theta},\boldsymbol{\varepsilon_c})$ is the radius of the admixed neutron star. Moreover, by assuming each of the mass-radius data sets are independent of one another and equating the mass-radius data sets to those derived from PPM, we obtain

$$p(\boldsymbol{\theta},\boldsymbol{\varepsilon_c}|\mathbf{d}) \propto p(\boldsymbol{\theta})p(\boldsymbol{\varepsilon_c}|\boldsymbol{\theta})\prod_i p(M_i,R_i|d_{PPM,i}), \tag{11}$$

where i runs over the number of stars for which PPM delivers the mass and radius and $d_{PPM,i}$ is an element in the $\mathbf{d}$ vector in which PPM was used. Furthermore, since the ADM mass-fraction is a function of baryonic and ADM EoS parameters and central energy densities, we can sample over the ADM mass-fraction instead of the ADM central energy density by introducing $F_\chi = F_\chi(\boldsymbol{\theta},\boldsymbol{\varepsilon_{c,B}},\boldsymbol{\varepsilon_{c,ADM}})$. This implies that the posterior distribution $\boldsymbol{\theta}$ and $\boldsymbol{\varepsilon_c}$ can be rewritten as

$$\begin{aligned} p(\boldsymbol{\theta},\boldsymbol{\varepsilon_{c,B}},\boldsymbol{F_\chi}|\mathbf{d}) &\propto p(\boldsymbol{\theta})p(\boldsymbol{\varepsilon_{c,B}}|\boldsymbol{\theta})p(\boldsymbol{F_\chi}|\boldsymbol{\theta},\boldsymbol{\varepsilon_c}) \\ &\quad\times\prod_i p(M_i,R_i|d_{PPM,i}), \end{aligned} \tag{12}$$

where $\boldsymbol{\varepsilon_{c,B}}$ and $\boldsymbol{\varepsilon_{c,ADM}}$ are the central energy densities of baryonic matter and ADM, respectively. Sampling over the ADM mass-fraction rather than the ADM central energy density allows for a direct comparison between the potential accumulation methods of ADM in neutron stars and the F_χ prior space.

B. Baryonic matter priors

We now define the priors on the baryonic matter EoS, which we describe using the parametrized PP EoS model used in [1,25–27,34] from Sec. II B. Since the neutron star crust is modeled after the fixed Baym-Pethick-Sutherland crust EoS [99], the prior ranges that need to be defined are those on the [1] χEFT band, the three polytropes, and the two varying transition densities between each polytrope. As described in Sec. II B, the [1] χEFT band is fitted between $0.5n_0$ and $1.1n_0$ using a single polytrope, which is of the form

$$P_{\chi\mathrm{EFT}}(n_B) = K(n_B/n_0)^\Gamma, \tag{13}$$

where $P_{\chi EFT}$ is the χEFT pressure as a function of baryonic number density n_B, K is the matching constant to $P_{\chi EFT}$ in units of MeV fm^{-3}, and Γ is the adiabatic index. Following the fitting procedure in [27], which fits the maximum and minimum pressure bands of a given χEFT using Eq. (13), the [1] band is well reproduced by $K \in [1.676, 2.814]$ MeV fm^{-3} and $\Gamma \in [2.486, 2.571]$. We take the fit parameters for K and Γ to be the prior bounds on the [1] χEFT band.

In order to produce the three polytropic priors, we consider the allowed ranges described in [1,97], which define the priors on the first polytropic index (Γ_1), the transition density between the first and second polytropes (n_1), the second polytropic index (Γ_2), the transition density between the second and third polytropes (n_2), and the third polytropic index (Γ_3). The priors on each parameter are given as $\Gamma_1 \in [1, 4.5]$, $\Gamma_2 \in [0., 8.]$, $\Gamma_3 \in [0.5, 8]$, and $1.5n_0 \leq n_1 < n_2 \leq 8.3n_0$. Here, the priors on Γ_1 in [1] are restricted to a smaller range relative to the other two polytropes because it controls the stiffness of the EoS between $1.1n_0 \leq n \leq 1.5n_0$, which is still well constrained by the [1] χEFT calculations. Therefore, in order to remain consistent with causality and with the χEFT band at $1.1n_0$, the variations in Γ_1 must be restricted to [1, 4.5] [1]. The priors of Γ_2 where chosen to allow for the possibility of a first-order phase transition (i.e., $\Gamma_2 = 0$), such as those in quark matter EoSs, and to capture the maximally stiff EoSs of this PP framework, which corresponds to $\Gamma_{2,\max} = 8$, which is determined by causality and a maximum neutron star mass of $3M_\odot$. For densities beyond n_2, the prior of Γ_3 is chosen similarly to Γ_2, but 0 is excluded to avoid numerical artifacts associated with a first-order phase transition in the density range of Γ_2. The transition densities between the three polytropes, n_1 and n_2, are allowed up to $8.3n_0$ as this is the maximal central density of the PP model [1,97]. Since each polytropic segment in the [1] PP model is determined by three parameters, K_i, Γ_i, and the number density n, then a prior on K_i must also be defined. However, according to [98], when an EoS is specified at lower density, continuity of pressure forces K_i to

---

[4] https://github.com/xpsi-group/neost

$$K_i = \frac{P(n_t)}{n_t^{\Gamma_i}}, \tag{14}$$

where n_t is the transition density. In this case the n_t's are set by the χEFT band for the first polytrope, n_1 for the second polytrope, and n_2 for the third polytrope. Last, for each PP EoS parameter, we uniformly sample the considered prior ranges.

C. Fermionic ADM priors

We now define the priors on each of the fermionic ADM EoS parameters. In particular, we use the available literature and physical constraints (if any) to construct the prior spaces on m_χ, F_χ, and g_χ/m_ϕ, all three of which completely define the fermionic ADM EoS.

To define the prior space on the fermionic ADM particle mass, we consider the physical constraints on m_χ from [78,105]. The considered lower bound on m_χ was obtained by [105], which showed that the minimum m_χ such that no ADM particle can exceed the neutron star escape velocity is

$$m_\chi \geq 10^{-2}\ \text{MeV}. \tag{15}$$

On the other hand, [78] considered fermionic ADM core collapse to a black hole inside the host neutron star. The authors showed that in order to avoid the formation of a black hole, regardless of whether the ADM is self-interacting,

$$m_\chi \leq 10^{9}\ \text{MeV}. \tag{16}$$

Therefore, the prior space on the fermionic ADM particle mass is defined by

$$m_\chi \in [10^{-2}\ \text{MeV}, 10^{9}\ \text{MeV}]. \tag{17}$$

While the prior space on the fermionic ADM particle mass is well constrained, the ADM mass-fraction prior space is not. Typically, the fermionic ADM mass-fraction prior space is defined using physically motivated ADM accumulation methods, such as neutron bremsstrahlung [40,51], production of ADM in supernovae [40,96], and neutron conversion to ADM [51,56,106]. The neutron bremsstrahlung reaction of ADM produces the gauge boson ϕ_μ via the conversion of the kinetic energy produced between the scattering of two neutrons (NN), i.e., $NN \longrightarrow NN\phi_\mu$. Moreover, since ϕ_μ is strongly coupled to ADM, the reaction of $NN \longrightarrow NN\bar{\chi}\chi$ proceeds at a similar rate as that of the neutron bremsstrahlung reaction.

In order to ensure that the ADM does not annihilate with the anti-ADM particles after the neutron bremsstrahlung reaction, Nelson *et al.* [40] assumed that anti-ADM is repulsed by baryonic matter and ADM is attracted to it. By making this assumption, Nelson *et al.* [40] showed that the energy difference of anti-ADM to ADM in the mean-field approximation is given by, in units of $\hbar = c = 1$,

$$\Delta E = E_{\bar{\chi}} - E_\chi = \frac{2 g_\chi g_B}{m_\phi^2} n_B, \tag{18}$$

where $E_{\bar{\chi}}$ is the energy of the anti-ADM particle, E_χ is the energy of the ADM particle, and n_B is the baryon number density. Thus, for the mass scales of m_ϕ for this model and when $g_B g_\chi \simeq 10^{-16}$–$10^{-10}$, ΔE is comparable to the gravitational binding energy of ADM/anti-ADM, which will preferentially trap the ADM particles and expel the anti-ADM particles. Thus, neutron bremsstrahlung provides a mechanism to produce and trap ADM inside neutron stars without having it diminished by annihilation, which allows for the maximum amount of ADM to be accumulated.

Since young neutron stars have temperatures around 50 MeV and assuming $m_\chi = 100$ MeV, neutron bremsstrahlung of ADM can produce $\approx 0.02 M_{NS}$, where M_{NS} is the mass of the neutron star [51]. Since neutrons inside compact objects can reach Fermi momenta of several hundred MeV, neutrons can decay to ADM for ADM particle masses less than $m_n + \mathcal{O}(k_{\mathrm{F},\chi}^2/2m_n)$, where m_n is the mass of the neutron. This process allows for total ADM masses of $\approx 0.05 M_{NS}$ [51,96]. Last, ADM can accumulate inside neutron stars via the production of ADM in supernovae. Since supernovae are very energetic events with luminosities in excess of $\mathcal{O}(10^{52}\ \text{erg/s})$, they can efficiently produce ADM particles that can then be trapped within the newly born neutron star. As discussed in [96], supernovae events can produce total accumulated ADM masses up to about $0.15 M_\odot$ for MeV-scale ADM particles.

Although neutron bremsstrahlung of ADM, neutron conversion of ADM, and production of ADM in supernovae each are capable of producing total ADM masses in the range of 0.02–$0.15 M_\odot$, all three of these processes are effective for ADM particle masses up to $\mathcal{O}(10^{2-3})$ MeV, which would only apply to a small fraction of the m_χ prior space. Since the aforementioned physically motivated mechanisms only apply to a few order magnitudes within the m_χ prior space, we choose to not consider these ADM accumulation methods within our F_χ prior space. Other accumulation methods, such as a neutron star passing through an ADM overdensity, accretion of baryonic matter onto a preexisting ADM core, and a dark star–neutron star merger, could be considered (see [54,96] and references therein). However, such ADM accumulation mechanisms are highly speculative, and thus we also neglect these accumulation methods. Therefore, to define the F_χ prior space, we follow the upper bound ADM mass-fraction estimate of [52] using the Navarro-Frenk-White dark matter mass density profile [107] to compute the local dark matter density around our considered sources. The Navarro-Frenk-White dark matter profile is given by

$$\rho_\chi(r) = \frac{\rho_0}{\frac{r_s}{r}(1+\frac{r}{r_s})^2}, \tag{19}$$

where $\rho_\chi(r)$ is the ADM mass density a radius, r, from the Galactic center (GC), $\rho_0 = 5.22 \pm 0.46 \times 10^7 M_\odot/\mathrm{kpc}^3$ is the central density [108], and $r_s = 8.1 \pm 0.7$ kpc is the scale radius [108]. By considering the F_χ approximation of [52], an upper limit on F_χ can be determined without a heavily restricted ADM particle mass prior space or having to consider a very hypothetical accumulation scenario.

In order to estimate the upper bound on F_χ, [52] calculated the ratio of the ADM mass density to the combined mass density of baryonic matter and ADM in the vicinity of PSR J0740 + 6620 and PSR J0348 + 0432, which are 8.6 and 9.9 kpc from the GC, respectively. To model the baryonic mass density distribution, [52] used only the contribution of the Milky Way's stellar disc because both pulsars were taken to be sufficiently far away from the Galactic bulge. The shape of Galactic stellar disc profile is

$$\rho_B(r) = \rho_{s,B} e^{-r/r_{s,B}}, \tag{20}$$

where $\rho_B(r)$ is the baryonic mass density as a function of r, from the GC, $\rho_{s,B} = 15 M_\odot/\mathrm{pc}^3$ is the baryonic mass density scale, and $r_{s,B} = 3.0$ kpc is the baryonic scale radius [109]. Since this work seeks to constrain fermionic ADM using neutron stars delivered by PPM, we only consider PSR J0740 + 6620. Using the radial distance of PSR J0740 + 6620 to the GC, [52] found the F_χ upper bound near PSR J0740 + 6620 to be $F_\chi \leq 1.7\%$. By repeating the F_χ upper bound estimation for the two other PPM sources from NICER, we find that the maximum possible ADM mass-fraction is $\leq$1.69% and $\leq$1.67% for PSR J0030 + 0451 and PSR J0437 − 4715, respectively. Note that we have found the radial distances to the GC to be 8.45 and 8.35 kpc, for PSR J0437 − 4715 and PSR J0030 + 0451, respectively. Therefore, because all three PPM delivered pulsars have similar F_χ upper estimates and PSR J0740 + 6620 can achieve the highest possible ADM mass-fraction, we adopt the upper bound on the ADM mass-fraction prior space to be

$$F_\chi \leq 1.7\%. \tag{21}$$

Last, we want to caution that the [52] calculation provides a best case upper estimate on F_χ in all of the NICER targets and that the true ADM mass-fraction in each pulsar due to their respective ADM surroundings is likely smaller than 1.7%.

Depending on the assumed ADM accumulation mechanism and scenario, the F_χ prior space can be constrained to be a finite size, but the effective fermionic ADM self-repulsion strength has yet to be physically constrained. In order to ensure that the g_χ/m_ϕ prior space is bounded from above, we adopt the upper bound of $g_\chi/m_\phi \leq 10^3\ \mathrm{MeV}^{-1}$ to capture the highest self-repulsion strengths used in [40]. From below, g_χ/m_ϕ is physically allowed to be zero because the ADM fermionic degeneracy pressure provides enough support against gravitational collapse to a black hole. However, in Sec. II B, we have additionally assumed that $g_B \ll g_\chi$, and thus a nonzero approximation to $g_\chi/m_\phi = 0\ \mathrm{MeV}^{-1}$ is necessary. To accomplish this, we compute the relative radial percent difference (RRPD) between 0 MeV^{-1} and a small nonzero self-repulsion for various baryonic matter EoSs and pairs of (m_χ, F_χ). We find that the RRPDs between $g_\chi/m_\phi = 10^{-5}\ \mathrm{MeV}^{-1}$ and zero self-repulsion do not exceed $4 \times 10^{-3}\%$. This shows that $10^{-5}\ \mathrm{MeV}^{-1}$ is an adequate approximation for 0 MeV^{-1} down to mass-radius measurements with uncertainties $\mathcal{O}(10^{-3}\%)$ (see the Appendix for further details).

In summary, the fermionic ADM EoS prior space is taken to be

$$\log_{10}(m_\chi/\mathrm{MeV}) \in [-2, 9], \tag{22}$$

$$F_\chi \in [0, 1.7]\%, \tag{23}$$

$$\log_{10}\left(\frac{g_\chi}{m_\phi/\mathrm{MeV}}\right) \in [-5, 3]. \tag{24}$$

Within each interval above, we uniformly sample each ADM parameter. We also assign all halo configurations to have a zero likelihood because the existence of any ADM halo has been shown to modify the pulse profile of neutron stars and thus the interpretation of the NICER mass-radius measurements [47]. This results in only ADM cores within the prior space. Moreover, within the remaining ADM core configurations, we also assign any ADM admixed neutron star with a mass $< 1 M_\odot$ to have a zero likelihood evaluation. The minimum neutron star mass constraint is motivated by the theoretical description of a newly born neutron star [110]. In addition, the $1 M_\odot$ constraint is compatible with the minimum neutron star remnant masses from core-collapse supernovae simulations (see e.g., [111,112]).[5] The consequences of the no-ADM halo and $1 M_\odot$ constraints can be seen as the nonshaded regions above and below the stripe in the $\log_{10}(g_\chi/(m_\phi/\mathrm{MeV}))$ vs $\log_{10}(m_\chi/\mathrm{MeV})$ plot of Fig. 1. In Fig. 1, we show the prior corner plots of fermionic ADM EoS parameters, which shows a nonuniform distribution for all three fermionic ADM EoS parameters.

---

[5] We also want to note that our imposed $1 M_\odot$ constraint, although well supported, is in tension with the mass-radius measurement of the HESS J1731 − 347 supernova remnant [113]. However, this measurement was challenged by [114] because the [113] analysis relied on several assumptions about the distance to the star, the spectral modeling, and the data set chosen in the analysis.

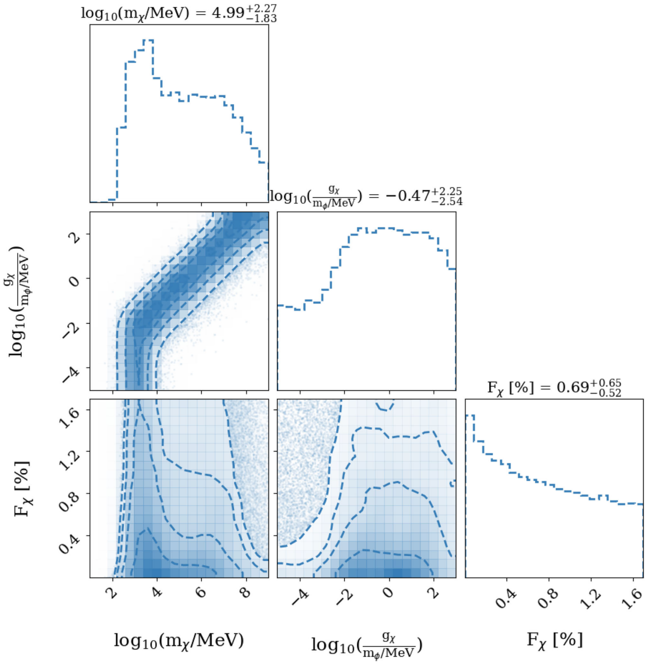

FIG. 1. Prior corner plot of the fermionic ADM EoS. Here, the ADM particle mass, effective self-interaction strength, and mass-fraction are plotted against each other, where the dark shaded regions represent a higher prior probability and lighter shaded regions represent a lower prior probability. The dashed blue lines in the 2D contour plots represent the 0.5, 1, 1.5, and 2σ contour levels. The top panels in each column show the 1D prior histogram. The figure titles on the diagonal show the median value with the 0.16 and 0.84 fractional quantiles. In the $\log_{10}(m_\chi/\mathrm{MeV}) - \log_{10}(g_\chi/(m_\phi/\mathrm{MeV}))$ plane we observe that the prior density has two large regions of no shading.

D. Source selection: Real and synthetic

By considering both real and synthetic data, we are able to demonstrate the current constraining power of NICER, and the potential future constraints of large-area x-ray telescopes, like STROBE-X.

In order to assess the current capabilities of PPM delivered measurements, we consider the mass-radius posteriors of the NICER targets PSR J0740 + 6620 from [14] and PSR J0030 + 0451 from [19]. In the top panel of Fig. 2, we show the mass-radius posteriors of PSR J0740 + 6620 of [14] and PSR J0030 + 0451 of [19] for our real data inferences.

Although the current mass-radius uncertainties on the NICER targets are at the ∼10% level, it is interesting to consider the impact of future measurements in which more neutron stars will be observed at significantly lower mass-radius uncertainties. For the inferences where we consider synthetic neutron star mass-radius measurements, we model our sources using the *Future-X* scenario of [83]. The *Future-X* scenario assumes six sources in the mass range of 1.2–2.2$M_\odot$ with mass-radius uncertainties at the 2% level. This scenario is modeled after a best-case possibility for the proposed NASA probe mission STROBE-X, where STROBE-X performs long targeted observations of the six best candidates. We expect this scenario to deliver uncertainties at the 2% level, which would provide the strongest constraints on the neutron star EoS. The bottom panel of Fig. 2 shows the uncertainty ellipses corresponding to the *Future-X* scenario.

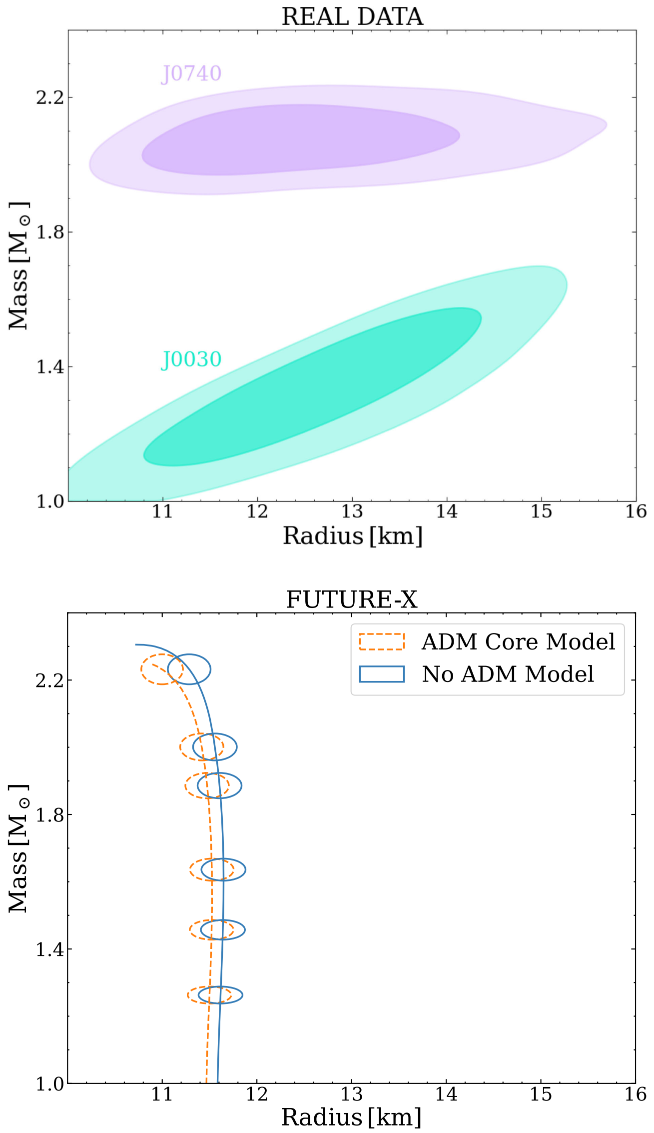

FIG. 2. Top panel: the 68% and 95% level uncertainty ellipses of the mass-radius measurements of PSR J0740 + 6620 from [14] and PSR J0030 + 0451 from [19]. Bottom panel: uncertainty ellipses from the 1σ level of the 2D Gaussian for each of the synthetic *Future-X* sources calculated from both ground truth models defined in Sec. IV B.

IV. RESULTS AND DISCUSSION

In all of our Bayesian parameter estimations, we take the most conservative approach of simultaneously varying all EoS parameters. By sampling all parameters in the neutron

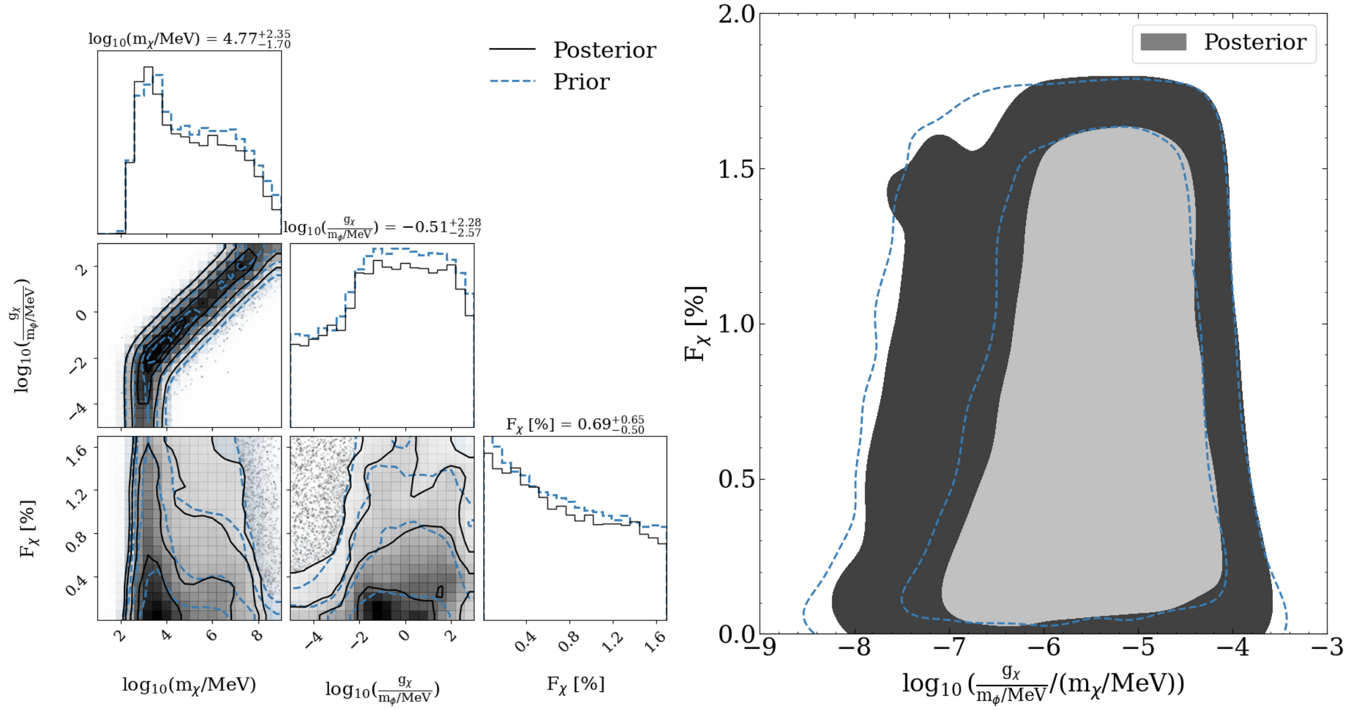

FIG. 3. Left panel: posterior distribution of the fermionic ADM EoS parameters (solid black lines) in which real data is considered. For comparison, we overlay the posteriors with their respective priors (dashed blue lines). The contour levels are the same as in Fig. 1. Right panel: probability density contour plot of the ADM posteriors in the F_χ vs $\log_{10}\left(\frac{g_\chi}{(m_\phi/\text{MeV})}/(m_\chi/\text{MeV})\right)$ plane. Note that the contours represent the 1σ (light gray) and 2σ (dark gray) levels for both the prior and posterior. Here we see that the 1σ level posteriors favor slightly higher ratios of g_χ/m_χ and m_χ, but the 2σ posteriors are almost touching the priors for all F_χ. In the left panel, we find that the priors and posteriors are nearly identical in all panels. However, in the right panel, we find that the 1σ and 2σ level posteriors favor slightly higher ratios of g_χ/m_χ and m_χ than their respective priors.

star EoS model, the most likely combined EoS of baryonic matter and fermionic ADM can be inferred. Additionally, this approach also allows for the constraints on the fermionic ADM EoS to be determined. In this section, we first study the posteriors of the fermionic ADM EoS and baryonic EoS using the mass-radius measurements of PSR J0740 + 6620 [14] and PSR J0030 + 0451 [19]. Using the synthetic data of the *Future-X* scenario, we again perform Bayesian inference on the fermionic ADM and baryonic matter EoSs to study the future promise of constraining fermionic ADM cores using neutron star mass-radius measurements.

A. Real data inferences

In Fig. 3, we show the posterior distributions on the fermionic ADM EoS in which we consider the mass-radius measurements of PSR J0740 + 6620 [14] and PSR J0030 + 0451 [19]. Here, the corner plot in the left panel of Fig. 3 shows that all of the 1D histograms and 2D posterior density contours strongly overlap with their respective priors. The strong overlap of the priors and posteriors on the fermionic ADM EoS parameters is due to the apparent degeneracy between the ADM EoS parameters. That is, varying both the baryonic matter and ADM EoSs allows for scenarios in which neutron stars with a baryonic EoS and an ADM core described by one set of (m_χ, g_χ/m_ϕ, F_χ) can be equally well described by a relatively similar baryonic EoS with an ADM core described by a different set (m'_χ, g'_χ/m_ϕ, F'_χ), which would give both sets of ADM parameters similar likelihoods. For example, a neutron star with an ADM core defined by ($m_\chi = 45$ GeV, $g_\chi/m_\phi = 0.01\,\text{Me}\,\text{V}^{-1}$, $F_\chi = 1\%$) radially differs by $<0.6\%$ from another ADM core with ($m_\chi = 0.5$ GeV, $g_\chi/m_\phi = 0.001\,\text{Me}\,\text{V}^{-1}$, $F_\chi = 1.7\%$). Therefore, because the radial difference between the two sets of parameters is much smaller than the $\mathcal{O}(10\%)$ measurement uncertainties, both sets will receive similar likelihood evaluations. From the observation that the fermionic ADM priors and posteriors are approximately identical, we conclude that the fermionic ADM EoS parameters cannot be constrained under the chosen priors and current uncertainties of the baryonic EoS.

If the fermionic ADM posteriors and priors are transformed into the $\log_{10}(\frac{g_\chi}{(m_\phi/\text{MeV})}/(m_\chi/\text{MeV}))$-$F_\chi$ plane (right panel of Fig. 3), we find that the lower bound on the ratio of g_χ/m_ϕ and m_χ can be constrained when compared to the prior. In particular, we find that the prior 68% (95%) credible level on $\log_{10}\left(\frac{g_\chi}{(m_\phi/\text{MeV})}/(m_\chi/\text{MeV})\right)$

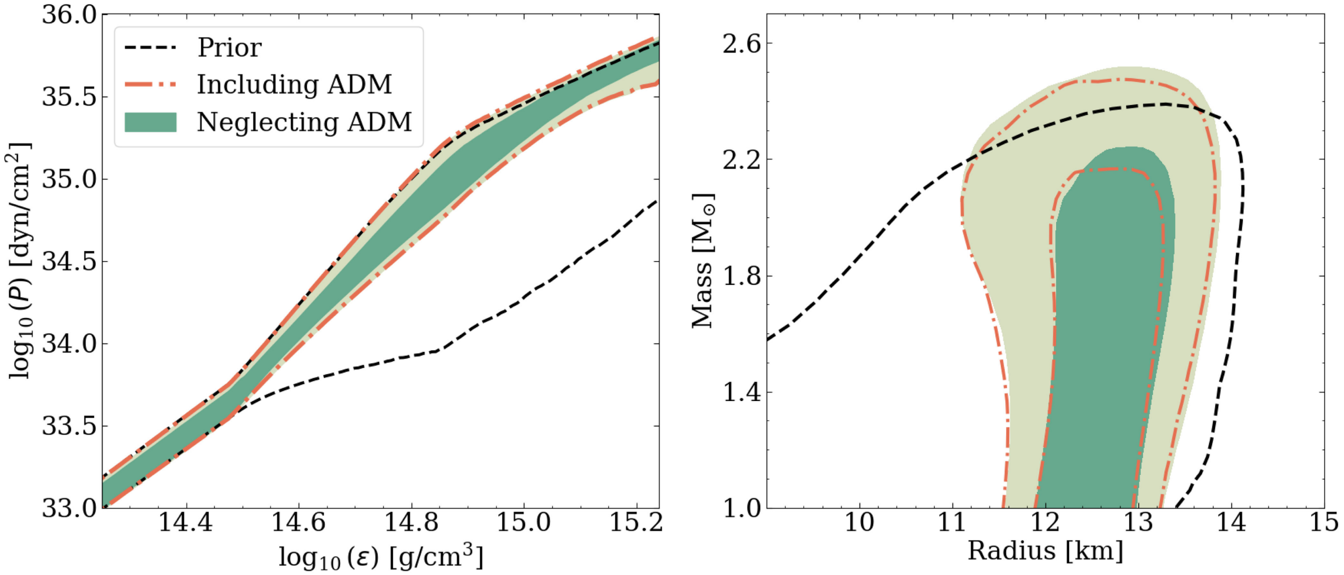

FIG. 4. Left panel: pressure-energy density posterior and prior distributions for the baryonic EoS for when fermionic ADM is included and neglected. Right panel: mass-radius posterior and prior distributions for the total combined ADM and baryonic EoSs for when fermionic ADM is included and neglected. For both panels, the black dashed line represents the 95% prior distribution, the orange dashed-dotted lines represent the 68% and 95% confidence regions of the posteriors that vary both the baryonic and fermionic ADM EoS parameters, and the light/dark green regions are the 68% and 95% confidence regions of the posteriors that only vary the baryonic EoS. Note that in the left panel we only show the 95% confidence region of the "Including ADM" band. Here we see that the "Including ADM" bands are nearly identical to the "Neglecting ADM" bands in both panels.

is $-5.7^{+1.08}_{-1.15}$ ($-5.7^{+1.62}_{-2.3}$). For the posteriors, we find the 68% (95%) credible level to be $-5.57^{+0.97}_{-1.02}$ ($-5.57^{+1.48}_{-2.2}$). Thus, the lower bound on $\log_{10}(\frac{g_\chi}{(m_\phi/\mathrm{MeV})}/(m_\chi/\mathrm{MeV}))$ can be constrained to -6.59 and -7.77 at the 68% and 95% credible levels, respectively. The lower bound on the ratio of g_χ/m_ϕ and m_χ can be constrained while the upper bound cannot because small ratios produce compact ADM cores with ADM central densities that are several orders of magnitude larger than the baryonic central densities for a given F_χ, which significantly reduce the resulting neutron star mass below the $1M_\odot$ constraint. However, for the same F_χ, large ratios of g_χ/m_ϕ and m_χ produce more diffuse fermionic ADM cores with ADM central densities less than baryonic central energy densities, which affect the overall neutron star mass less than the lower ratios. For instance, for $\log_{10}(\frac{g_\chi}{(m_\phi/\mathrm{MeV})}/(m_\chi/\mathrm{MeV})) = -8$ and $F_\chi = 0.75\%$, the maximum central ADM density is $\approx 10^{20}$ g/cm^3 and the maximum central baryonic density is $\approx 10^{15}$ g/cm^3, which results in the maximum neutron star mass of $\approx 0.86 M_\odot$. However, if we again take $F_\chi = 0.75\%$ and the same maximum baryonic central density, but $\log_{10}(\frac{g_\chi}{(m_\phi/\mathrm{MeV})}/(m_\chi/\mathrm{MeV})) = -4$, the maximum central ADM density is reduced to $\approx 10^{13.4}$ g/cm^3 and the maximum neutron star mass increases to $2.38 M_\odot$.

In Fig. 4, the priors and posteriors of Fig. 3 are converted to the pressure-energy density plane (left) to study the effect that fermionic ADM cores have on the uncertainties of the baryonic EoS.[6] In particular, we consider the posteriors that only vary the baryonic EoS parameters ("Neglecting ADM") and the posteriors that vary the combined ADM and baryonic matter EoS parameters ("Including ADM"). Figure 4 shows that the 95% confidence region of the "Including ADM" band (orange dashed dotted band) is marginally wider than the 95% confidence region of the "Neglecting ADM" band (light green band). Quantitatively, we calculate that the "Including ADM" band is 1.021% and 1.025% wider than the "Neglecting ADM" band at $\log_{10}(\varepsilon\ \mathrm{cm}^3/\mathrm{g}) = 14.381$ and $\log_{10}(\varepsilon\ \mathrm{cm}^3/\mathrm{g}) = 15.010$, respectively. Accounting for the possibility of fermionic ADM cores broadens the uncertainties on the baryonic EoS because ADM cores decrease the neutron star mass and radius, which allows the baryonic EoS to be more stiff and remain in agreement with the source data. However, since including fermionic ADM broadens the 95% confidence interval on the baryonic EoS by $\mathcal{O}(1\%)$, we conclude that fermionic ADM cores do not significantly impact the uncertainties on the baryonic EoS within the considered ADM priors.

Figure 4 additionally shows the posterior distributions on both the fermionic ADM admixed neutron star mass-radius relation ("Including ADM") and the purely baryonic mass-radius relation ("Neglecting ADM"). Along the radial axis,

---

[6] Note that we have scaled the energy density by a factor of c^{-2} such that it has units of g/cm^3.

Fig. 4 shows that the "Including ADM" contours predict similar radii to the "Neglecting ADM" contours. Figure 4 also shows that the "Including ADM" band favors marginally lower maximum masses than the "Neglecting ADM" band. In particular, the 68% and 95% confidence regions of the "Including ADM" band predict maximum masses of $2.167M_{\odot}$ and $2.475M_{\odot}$, respectively, while the "Neglecting ADM" band predicts maximum masses of $2.241M_{\odot}$ and $2.518M_{\odot}$ for the 68% and 95% confidence regions, respectively. The "Including ADM" posterior favors lower maximum masses than the "Neglecting ADM" posterior because ADM cores decrease neutron star masses when compared to an identical neutron star with the same baryonic central energy density. This reduction in mass from the presence of ADM cores would push the posteriors to predict lower maximum masses than inferences done with only baryonic matter. Since the "Including ADM" band only marginally favors lower maximum masses and strongly overlaps with the "Neglecting ADM" band, we find that the inclusion of fermionic ADM cores is equally as consistent with the NICER data as the posteriors which only account for baryonic matter.

B. Synthetic data inferences

We now consider the synthetic mass-radius measurements of a potential STROBE-X scenario using the *Future-X* scenario of [83]. To study such a potential scenario, it is useful to define two ground truth models i.e., models in which the synthetic neutron star mass-radius measurements will be computed: one with an ADM core and one with only baryonic matter. Considering two ground truth models allows for statements about the ADM EoS, regardless of whether ADM cores are actually present in neutron stars. The first ground truth model that we consider is the "ADM Core" model, which is described by the PP model in Sec. II B with an ADM core defined by the ADM parameters

$$m_{\chi} = 15\ \mathrm{GeV}, \tag{25}$$

$$\frac{g_{\chi}}{m_{\phi}/\mathrm{MeV}} = 0.01, \tag{26}$$

$$F_{\chi} = 1.5\%. \tag{27}$$

The second ground truth model is defined identically to the "ADM core" model, but $F_{\chi} = 0\%$ in order to account for the possibility that neutron stars do not accumulate an appreciable total ADM mass, but the possibility of ADM is still considered during sampling. Using the *Future-X* scenario with the "No ADM" and "ADM core" models in this way allows for the best-case future constraints on fermionic ADM to be determined (see [83]). In Fig. 2, the uncertainty ellipses and ground truth models for the *Future-X* scenario are shown.

In Fig. 5, we show the fermionic ADM prior and posterior distributions of the "No ADM" (left) and "ADM Core" (right) models for the *Future-X* scenario. In the top two panels, we show the corner plots of the "No ADM" and "ADM Core" models. In both the 2D density and 1D histograms plots, the posteriors of both ground truth models are identical to each other, despite having different ground truth ADM mass-fractions. In addition, the posterior distributions of the "ADM Core" and "No ADM" models are approximately identical to the prior distribution. Since the corner plots of both the "No ADM" and "ADM Core" models are nearly identical to each other as well as the prior, the *Future-X* scenario will not be able to provide any additional constraints on the fermionic ADM particle mass, effective self-repulsion strength, and mass-fraction than the inferences using the neutron star data from [14,19].

In the bottom two panels of Fig. 5, the fermionic ADM posteriors and priors are transformed to the $\log_{10}(\frac{g_{\chi}}{m_{\phi}/\mathrm{MeV}}/(m_{\chi}/\mathrm{MeV}))$-$F_{\chi}$ plane. Figure 5 shows that the "ADM Core" model posteriors narrow on the left side more than the "No ADM" posteriors for increasing F_{χ}. The posteriors on the ratio of g_{χ}/m_{ϕ} and m_{χ} differ along the F_{χ} axis because the ground truth mass-fractions are 1.5% and 0% for the "ADM Core" and "No ADM" models, respectively. That is, a given ratio of g_{χ}/m_{ϕ} and m_{χ} could produce mass-radius curves satisfying the "No ADM" model data for F_{χ} near 0%, but simultaneously not produce neutron stars satisfying the "ADM Core" model data for $F_{\chi} \approx 1.5\%$. Since the posteriors on the ratio of the fermionic ADM self-repulsion and particle mass differ between both ground truth models and the priors, we find that *Future-X* will be able to constrain the lower bound on the ratio of g_{χ}/m_{ϕ} and m_{χ}. In particular, the lower bound on $\log_{10}(\frac{g_{\chi}}{m_{\phi}/\mathrm{MeV}}/(m_{\chi}/\mathrm{MeV}))$ is constrained to be $\gtrsim -6.49$ and $\gtrsim -7.68$, at the 68% and 95% confidence intervals, respectively. However, when compared to the real data posteriors of Fig. 3, the *Future-X* scenario can only slightly tighten the constraints on $\log_{10}(\frac{g_{\chi}}{m_{\phi}/\mathrm{MeV}}/(m_{\chi}/\mathrm{MeV}))$ at both the 68% and 95% confidence intervals.

Figure 6 shows the "No ADM" and "ADM Core" model posteriors on the baryonic EoS uncertainty in the pressure-energy density plane (top two panels) and the combined fermionic ADM and baryonic matter EoS in the mass-radius plane (bottom two panels). In the pressure-energy density plane, the 95% confidence region of the "Including ADM" band predicts baryonic EoS uncertainties that are comparable to those of the "Neglecting ADM" band for both the "No ADM" and "ADM Core" models. In the mass-radius plane, the 68% and 95% confidence intervals on the "Including ADM" band also do not significantly deviate from their corresponding "Neglecting ADM" bands. The strong overlap between the "Neglecting ADM" and "Including ADM" posteriors is due to an apparent degeneracy between the fermionic ADM and baryonic matter

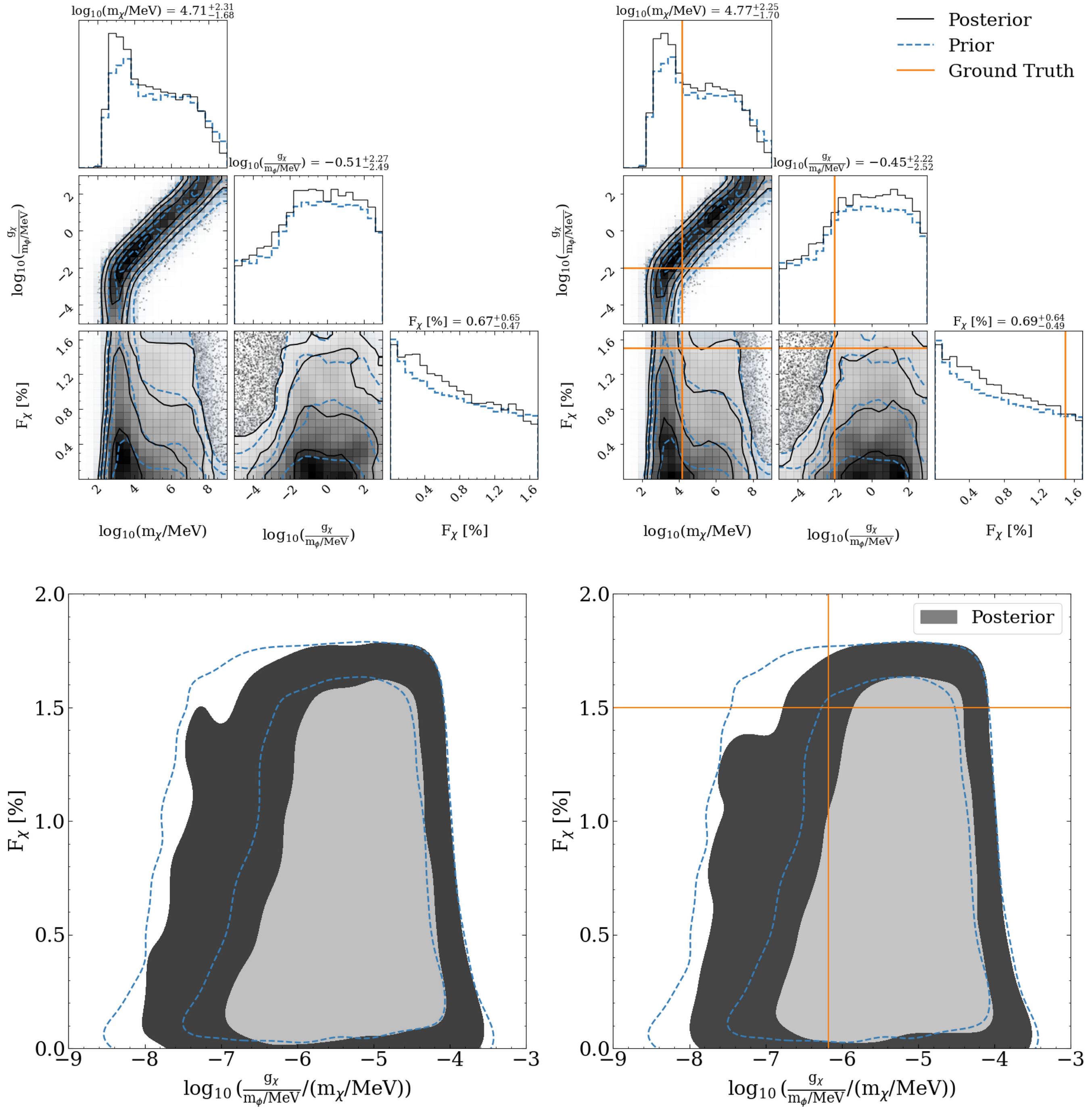

FIG. 5. Left two panels: *Future-X* fermionic ADM posteriors for the "No ADM" model. Right two panels: same as the left two panels, but for the "ADM Core" model. The top two panels are the corner plots of the fermionic ADM EoS posteriors for the "No ADM" and "ADM Core" ground truth models. The posterior and prior contour levels of the upper panels are same as in Fig. 3. In the bottom panels, we show the fermionic ADM posteriors and priors in the $\log_{10}(\frac{g_\chi}{m_\phi/\mathrm{MeV}}/(m_\chi/\mathrm{MeV}))$-$F_\chi$ plane. The contour levels of both the priors and posteriors are identical to the levels of Fig. 3. In all panels, the orange solid lines represent the ground truth values for the "ADM Core" model. We find that the corner plots of both ground truth models are approximately identical to one another, while the bottom contour plots differ slightly along the F_χ axis.

EoSs. Moreover, a strong degeneracy between fermionic ADM and baryonic matter implies that a stiff baryonic EoS with an ADM core can yield an identical mass-radius relation to a relatively softer baryonic EoS without an ADM core, which would result in both neutron star models receiving the same likelihood evaluations. Based on the observations that the "Including ADM" bands favor nearly identical posteriors to the "Neglecting ADM" bands, this

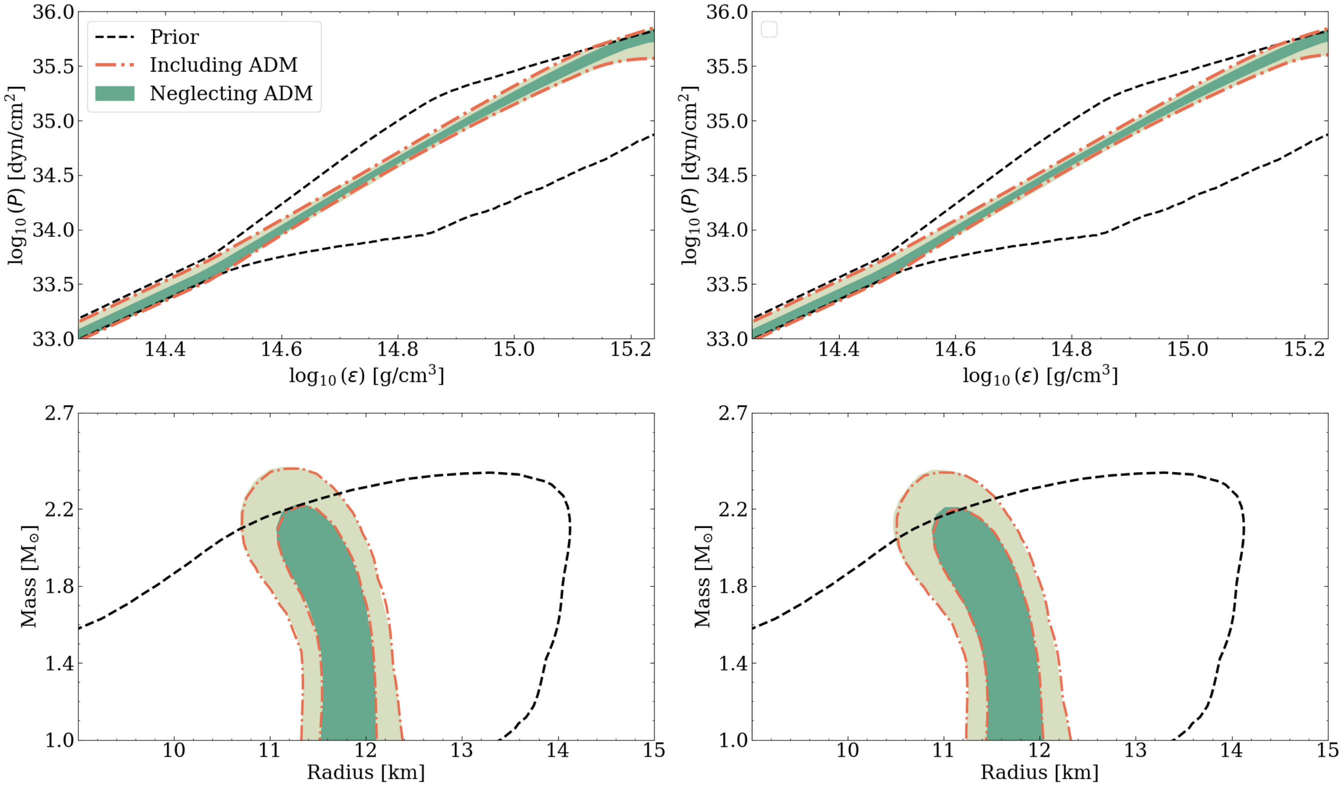

FIG. 6. Left two panels: *Future-X* fermionic ADM and baryonic matter EoS posteriors and priors of the “No ADM” model converted to the pressure-energy density plane (top panel) and mass-radius plane. Right two panels: same as the left two panels, but for the “ADM Core” model. Note that the top two panels follow the same legend and contour levels as Fig. 4, and the bottom two follow the same legend and contour levels as Fig. 5. Note that the solid orange lines in the bottom two panels are the “No ADM” and “ADM Core” model ground truth mass-radius curves, respectively. In all quadrants, we find that the “Including ADM” bands are nearly identical to the “Neglecting ADM” bands.

figure shows that neutron stars with fermionic ADM cores are indistinguishable from purely baryonic neutron stars. Thus, we conclude that the presence of fermionic ADM cores inside neutron stars is fully consistent with purely baryonic neutron stars down to the 2% mass-radius uncertainty level.

V. SUMMARY AND CONCLUSIONS

In this work, we have presented a full Bayesian analysis for fermionic ADM cores in neutron stars using the framework developed in [83]. Here we have modeled the fermionic ADM cores using the [40] ADM model, which describes ADM as spin $-1/2$ fermions with repulsive self-interactions. We have considered the mass-radius data of PSR J0740 + 6620 [14] and PSR J0030 + 0451 [19] as well as synthetic mass-radius data from a best-case scenario of the NASA STROBE-X mission. By considering both real and synthetic mass-radius measurements, we inferred the current and possible future constraints on the fermionic ADM particle mass m_χ, effective self-repulsion strength g_χ/m_ϕ, and mass-fraction F_χ.

For the inferences which consider the PSR J0740 + 6620 and PSR J0030 + 0451 mass-radius measurements, we found that the 2D posterior densities of $\log_{10}(m_\chi/\mathrm{MeV})\mathrm{vs}\log_{10}(g_\chi/(m_\phi/\mathrm{MeV}))$, $F_\chi \mathrm{vs}\log_{10}(m_\chi/\mathrm{MeV})$, and $F_\chi \mathrm{vs}\log_{10}(g_\chi/(m_\phi/\mathrm{MeV}))$ are nearly identical to their respective prior densities. In addition, the 1D posterior histograms of each fermionic ADM EoS parameter also strongly coincide with their prior counterparts. The fermionic ADM EoS posteriors are nearly identical to their corresponding priors because the EoS parameters are degenerate with one another such that one set of $(m_\chi,\, g_\chi/m_\phi,\, F_\chi)$ produces similar neutron stars as another set of $(m'_\chi,\, g'_\chi/m_\phi,\, F'_\chi)$. Thus, we conclude that the fermionic ADM EoS parameters cannot be constrained using the NICER mass-radius measurements of PSR J0740 + 6620 and PSR J0030 + 0451. If the ADM posteriors are transformed to the $\log_{10}(\frac{g_\chi}{m_\phi/\mathrm{MeV}}/(m_\chi/\mathrm{MeV}))$-$F_\chi$ plane, the lower bound on the ratio of the fermionic ADM effective self-repulsion strength to the particle mass can be constrained to -6.59 and -7.77 at the 68% and 95% confidence levels, respectively. These results show that, within the current uncertainties of neutron star mass-radius measurements delivered by NICER, the lower bound of the ratio of g_χ/m_ϕ and m_χ can only be marginally constrained. However, all other combinations of fermionic ADM parameters cannot be constrained.

Converting the fermionic ADM and baryonic matter EoS posteriors to the mass-radius and pressure-energy density planes, we find that the posteriors on the neutron star EoS are largely unaffected by the inclusion of fermionic ADM cores. In the mass-radius plane, we find that the maximum masses of the posteriors which include fermionic ADM differ from the purely baryonic ones at the 95% percent level by $0.0043 M_\odot$. Moreover, the combined fermionic ADM and baryonic mass-radius posteriors predict similar radii to the purely baryonic posteriors. In the pressure-energy density plane, the baryonic EoS uncertainty slightly broadens when fermionic ADM is accounted for. In particular, at $\log_{10}(\varepsilon\ \mathrm{cm}^3/\mathrm{g}) = 14.381$ and, the baryonic EoS uncertainty widens by 1.021%. The small differences between the posteriors that include fermionic ADM cores and the ones that do not, show that fermionic ADM cores inside neutron star interiors can be fully consistent with their purely baryonic counterparts.

In order to determine the promise of constraining fermionic ADM cores by missions, like the NASA STROBE-X mission, this work has also considered the *Future-X* scenario from [83]. The *Future-X* scenario describes six synthetic neutron star mass-radius measurements with mass and radius uncertainties at the 2% level. Within the *Future-X* scenario, the fermionic ADM posteriors remain nearly identical to the real data inferences for both the "ADM core" and "No ADM" models. However, we found that the posteriors on the ratio of g_χ/m_ϕ and m_χ differ between the "No ADM" and "ADM core" models. In particular, the "ADM core" model infers marginally tighter constraints on the lower bound of $\log_{10}(\frac{g_\chi}{m_\phi/\mathrm{MeV}}/(m_\chi/\mathrm{MeV}))$ than the "No ADM" model. The posteriors on the lower bound of $\log_{10}(\frac{g_\chi}{m_\phi/\mathrm{MeV}}/(m_\chi/\mathrm{MeV}))$ are slightly more narrow in the "ADM core" model than in the "No ADM" model because the ground truth mass-fraction of the "ADM core" model is higher than that of the "No ADM" model. This allows for ratios of g_χ/m_ϕ and m_χ, which produce neutron stars satisfying the "No ADM" data for a given F_χ, to be given a nonzero likelihood. However, the same ratios of g_χ/m_ϕ and m_χ would be given a zero likelihood because they would not satisfy the data of the "ADM core" model for the same given F_χ. Since the posteriors in the $\log_{10}(\frac{g_\chi}{m_\phi/\mathrm{MeV}}/(m_\chi/\mathrm{MeV}))$-$F_\chi$ plane differ between the "No ADM" and "ADM core" models, we found that *Future-X* will be able to constrain the lower bound of the ratio of g_χ/m_ϕ and m_χ.

According to the posteriors on the lower bound of the ratio of g_χ/m_ϕ and m_χ, we found that *Future-X* slightly tightens the constraints to -6.49 and -7.68 at the 68% and 95% confidence levels, respectively. It is physically reasonable that the constraints on $\log_{10}(\frac{g_\chi}{m_\phi/\mathrm{MeV}}/(m_\chi/\mathrm{MeV}))$ improve in the *Future-X* scenario because the mass of an admixed neutron star is sensitive to the compactness of the fermionic ADM core, which is partially controlled by the ratio of g_χ/m_ϕ and m_χ. Therefore, the posteriors on the lower bound of $\log_{10}(\frac{g_\chi}{m_\phi/\mathrm{MeV}}/(m_\chi/\mathrm{MeV}))$ will slightly improve with the tighter mass and radius uncertainties of the *Future-X* scenario. Note, however, that the *Future-X* scenario is a best-case scenario for the STROBE-X mission and our constraints will relax accordingly for larger mass-radius credible intervals.

In the pressure-energy density and mass-radius planes, we found that the uncertainties on the baryonic matter EoS and the total neutron star mass-radius remain unaffected when the possibility of fermionic ADM cores is considered. That is, similar to the real data inferences, we found that the pressure-energy density and mass-radius of the "Including ADM" bands are identical to their respective "Neglecting ADM" bands in both the "No ADM" and "ADM core" models. Our results highlight that neutron star EoS models that additionally allow for fermionic ADM cores are indistinguishable from the baryonic EoS inferences for mass and radius uncertainties down to the 2% level, which implies that ADM admixed neutron stars are equally as consistent with neutron star data as purely baryonic neutron stars.

The "Including ADM" posteriors in the pressure-energy density and mass-radius planes of both the real data from NICER and the hypothetical data from the *Future-X* scenario (STROBE-X) strongly coincide with their corresponding "Neglecting ADM" posteriors in part because, under the ADM mass-fraction priors considered, the presence of ADM cores does not significantly affect the uncertainties of the baryonic EoS. This is most clearly shown in Fig. 2, where the "ADM core" and "NO ADM" mass-radius relations are closely aligned. The other reason why including fermionic ADM cores is physically consistent with the purely baryonic matter posteriors is because of the strong degeneracy between the ADM and baryonic matter EoSs. That is, the mass-radius relation can be equally well described by both a stiff baryonic EoS with an ADM core and a softer baryonic EoS without ADM. Our results show this in the mass-radius posteriors of Figs. 4 and 6, where the purely baryonic posteriors strongly overlap with the fermionic ADM posteriors. Last, [63] pointed out several scenarios that could break this degeneracy, such as a reduction of neutron star masses toward the center of the Galaxy, searching for supplementary peaks in gravitational wave spectra from binary neutron star merger simulations, detecting objects that are in contrast to our understanding of neutron star structure, and by finding a new feature in the binary Love relation.

Overall, this work shows that the current neutron star measurement of the NASA NICER mission, as well as the potential future measurements of the NASA STROBE-X mission, can provide constraints on the lower bound of the ratio of g_χ/m_ϕ and m_χ, but not the individual quantities F_χ, m_χ, and g_χ/m_ϕ. Moreover, within the uncertainties on the baryonic EoS, neutron stars with ADM cores are equally consistent with the mass-radius data as stars only made of baryonic matter, which means that neither NICER nor STROBE-X will be able to distinguish between neutron stars with an ADM core and those without. Although fermionic ADM cores inside neutron stars are indistinguishable from their purely baryonic counterparts to NICER and STROBE-X, when specific assumptions about the neutron EoSs are made, small ADM mass-fractions have been shown to trigger rapid neutron star cooling for low-mass neutron stars through the direct Urca process, which could shed light on the presence of ADM in these stars [57,115,116].

In a similar analysis, [48] inferred that the ADM particle mass favors masses near 0.6 GeV for ADM cores using a fixed baryonic EoS with the NICER PSR J0740 + 6620 and PSR J0030 + 0451 measurements, which is in contrast with the findings of this work. However, when comparing our respective priors on m_χ, we observe that their priors are flat while ours are not. The observed difference between our priors and theirs could be due to the fact that our analysis strictly enforces a minimum neutron star mass constraint of $1M_\odot$, while the analysis of [48] does not specify one. Imposing a minimum neutron star mass constraint modifies the priors on the ADM parameters, which in-turn can modify the interpretation of the ADM posteriors. Moreover, [48] fixed their analysis to one baryonic EoS while our work varied the baryonic EoS, which can also change the ADM EoS posteriors (see e.g., [83]).

Another recent work, [45], considered ten different choices of baryonic matter EoS and a fermionic ADM model with self-interactions mediated by both a massive scalar and vector mediator. By directly comparing the mass-radius relations of the ten baryonic EoSs for a range of m_χ and ADM Fermi momenta values with the 95% contours of the NICER and LIGO/VIRGO, measurements, [45] found that $m_\chi \in [0.1, 30]$ GeV for Fermi momenta in the range of [0.01,0.07] GeV is consistent with the observational data. Our results differ from those of [45] for two key reasons. The first reason is that our analysis fully varied the baryonic EoS and considered the full distribution of the NICER PSR J0740 + 6620 and PSR J0030 + 0451 mass-radius posteriors as part of our analysis. Reference [45], by contrast, approximated the baryonic EoS uncertainty by considering ten representative choices and used the NICER and LIGO/VIRGO posterior contours as hard cutoffs. Although the approach of [45] had the advantage of determining tight constraints for a handful of fixed baryonic EoSs, our Bayesian analysis was less dependent on the baryonic EoS because it varied both the ADM and baryonic EoS during inference, allowing the most likely combination of ADM and baryonic matter to be determined. The second is that our analysis directly considered the ADM mass-fraction while [45] considered the ADM Fermi momentum, which can result in $F_\chi \gtrsim 50\%$ for many combinations of ADM parameters and different F_χ along the entire admixed mass-radius relation. Therefore, it is physically reasonable that the results of [45] more tightly constrained m_χ than this work because, in combination with choosing ten fixed baryonic EoSs, large F_χ will increasingly significantly affect the resulting mass-radius relation as m_χ increases, which will preferentially favor lower m_χ. However, our analysis allows for relatively smaller, and physically grounded, values of F_χ, which, of course, affect the resulting mass-radius relation less.

Finally, future work will explore how the proper inclusion of fermionic (as well as bosonic) ADM halos affects our inferences on both the ADM and baryonic matter EoSs. The work of [47] constructed a framework for interpreting neutron star mass-radius measurements in the presence of ADM halos. While many works considered a variety of different plausible ADM mass-fractions (see e.g., [47–49,51,54,58,61,96,117] and references therein), an in-depth analysis of the possible accumulation methods of ADM in neutron stars has yet to be done and is left for future work. By appropriately accounting for the possible presence of ADM halos and physically constraining F_χ, full inferences on the neutron star EoS will be able to determine the most general constraints on the ADM EoS.

Software used for the development of this article include Python/C language [118], GNU Scientific Library [119], NumPy [120], Cython [121], SciPy [122], MPI for Python [123], Matplotlib [124], Jupyter [125], MultiNest [126], PyMultiNest [127], KALEPY [128], CORNER [129], SEABORN [130], and NEoST [103].

ACKNOWLEDGMENTS

We acknowledge Ann Nelson for her pioneering work on dark matter in neutron stars. We thank Michael Lathwood for insightful conversations with N. R. on the consequences of the symmetric nature of the metric tensor. We also thank Nathan Musoke, Yves Kini, Anthony Mirasola, and Melissa Mendes for feedback on the manuscript. Last, we thank the anonymous referee for comments that helped improve this work. A. W. acknowledges support from ERC Consolidator Grant No. 865768 AEONS. C. P.-W. acknowledges all the administrative and facilities staff at the University of New Hampshire, especially Katie Makem-Boucher and Michelle Mancini. The contributions of C. P.-W. and N. R. were supported by NASA Grant No. 80NSSC22K0092.

DATA AVAILABILITY

The data that support the findings of this article are openly available [103,104].

APPENDIX: APPROXIMATING $g_\chi/m_\phi = 0\ \mathrm{MeV}^{-1}$

In order to capture the physically allowed parameter space of the effective fermionic self-repulsion strength, $g_\chi/m_\phi = 0\ \mathrm{MeV}^{-1}$ must be considered. However, since we have assumed $g_B \ll g_\chi$ (see Sec. III C), a nonzero approximation of $g_\chi/m_\phi = 0\ \mathrm{MeV}^{-1}$ is necessary. Here we approximate zero self-repulsion strength by calculating the average RRPD between the mass-radius curves of zero self-repulsion and a nonzero self-repulsion strength, which we take to be $10^{-5}\ \mathrm{MeV}^{-1}$, for all neutron star masses $\geq 1 M_\odot$. We define the RRPD at a fixed neutron star mass as

$$\mathrm{RRPD} = \frac{|R_{-5} - R_0|}{R_0} \cdot 100, \qquad \text{(A1)}$$

where R_{-5} is the radius of the neutron star produced by $g_\chi/m_\phi = 10^{-5}\ \mathrm{MeV}^{-1}$ and R_0 is the radius of the neutron star produced by zero self-repulsion strength.

To calculate the average RRPD values between the mass-radius relations with zero self-repulsion and $g_\chi/m_\phi = 10^{-5}\ \mathrm{MeV}^{-1}$ in a given interval of m_χ and F_χ for a fixed baryonic EoS, we adopt the following procedure. First, we compute the entire mass-radius relation for both

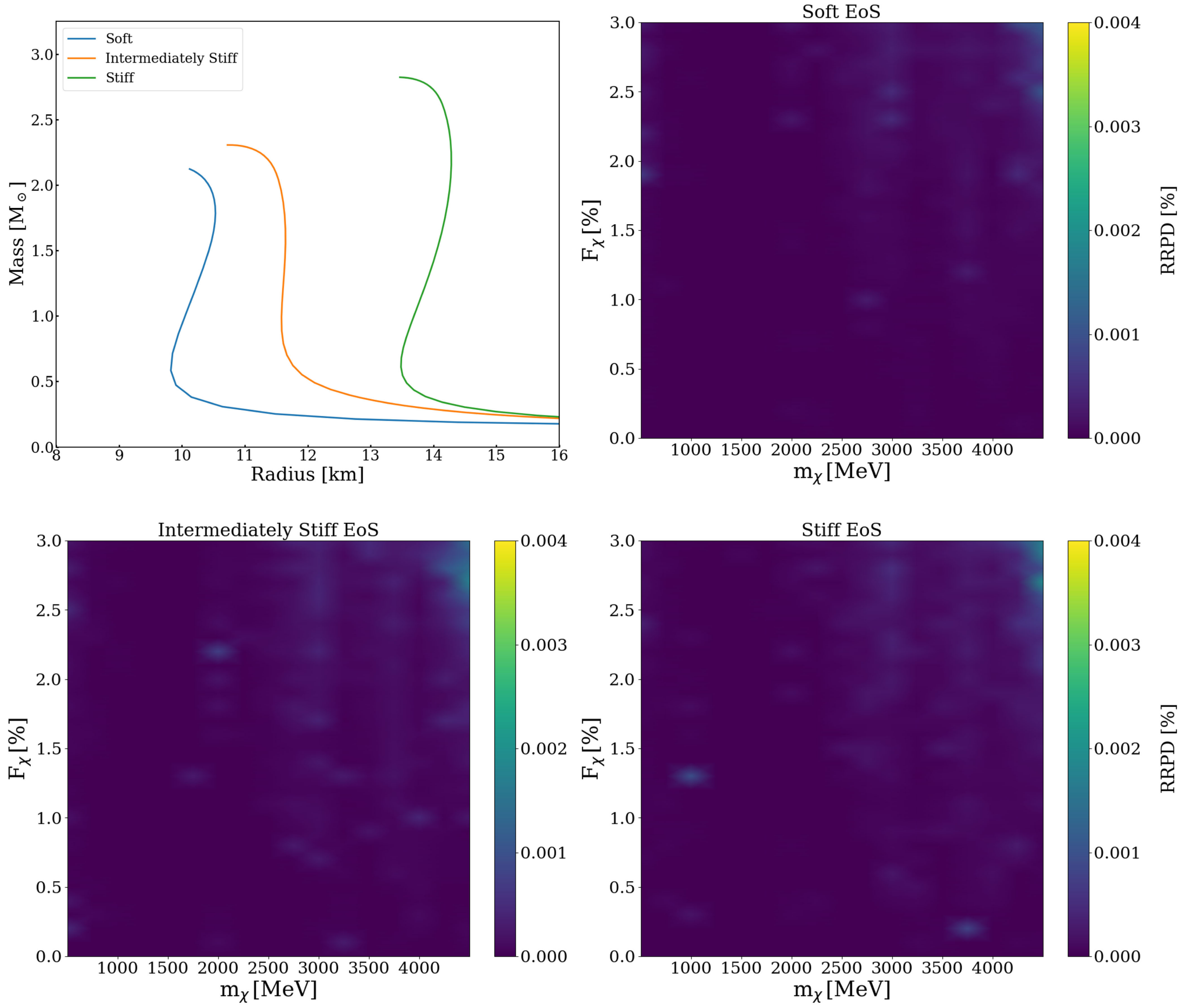

FIG. 7. Top Left: The three underlying baryonic mass-radius curves of varying stiffness from soft (left most blue) to intermediately stiff (middle orange) to stiff (right most green) used in the remaining three panels, respectively; Top Right: Color plot of the RRPD between $g_\chi/m_\phi = 0\ \mathrm{MeV}^{-1}$ and $g_\chi/m_\phi = 10^{-5}\ \mathrm{MeV}^{-1}$ in the ADM mass-fraction and particle mass plane for the Soft baryonic EoS; Bottom Left: Same as the top right panel, but for the intermediately stiff baryonic EoS; Bottom Right: Same as the top right panel, but for the stiff baryonic EoS. In all Color plots, the dark to light shading indicates an increase in RRPD value. For the top right panel and the bottom two panels, the RRPD values do not exceed 0.004%.

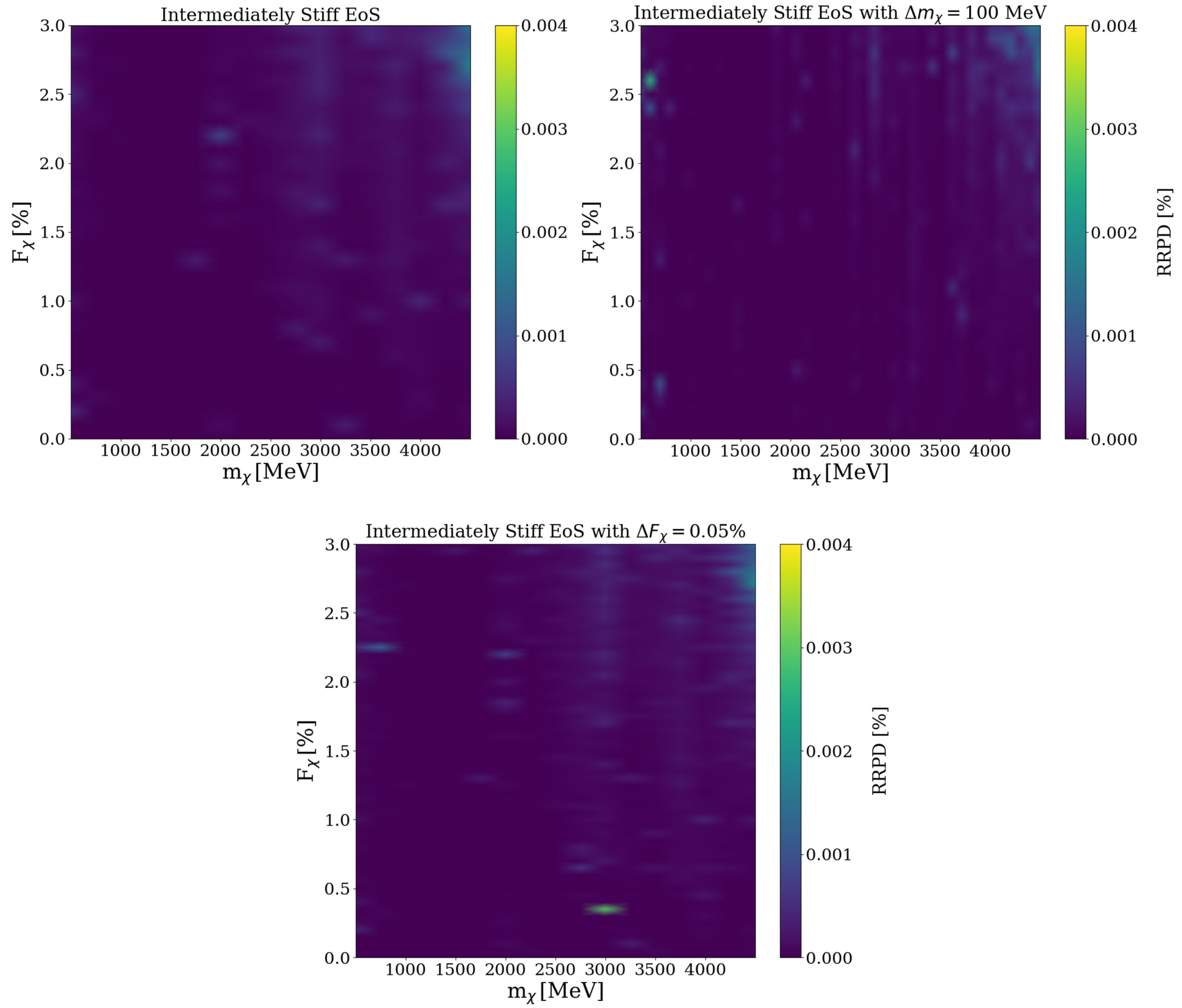
Intermediately Stiff EoS

Intermediately Stiff EoS with $\Delta m_\chi = 100$ MeV

Intermediately Stiff EoS with $\Delta F_\chi = 0.05\%$

FIG. 8. Top left: RRPD color plot in the ADM mass-fraction and particle mass plane for the intermediately stiff EoS. Top right: same as the top left panel, but the step size along the m_χ axis is changed from 250 to 100 MeV. Bottom: same as the top left panel, but the step size along the F_χ axis is changed from 0.1% to 0.05%. For all three panels, the maximum RRPD value does not exceed 0.004%.

$g_\chi/m_\phi = 10^{-5}$ MeV^{-1} and $g_\chi/m_\phi = 0$ MeV^{-1} for fixed m_χ and F_χ. Second, we linearly interpolate both mass-radius relations to obtain $R(M)$, i.e., neutron star radius as a function of gravitational mass. With $R(M)$ in hand, a direct comparison of identical masses between both mass-radius relations can made. Third, we draw 20 evenly spaced masses from $1M_\odot$ to the maximum mass of the two mass-radius curves and compute the RRPD for all 20 masses. Fourth, we average over the RRPD values of all masses $>1M_\odot$ and save the average value. Finally, steps 1–4 are repeated until the averaged RRPD value of each combination of m_χ and F_χ is obtained.

Using the above procedure to calculate the average RRPD values between $g_\chi/m_\phi = 0$ MeV^{-1} and $g_\chi/m_\phi = 10^{-5}$ MeV^{-1}, we compute the average RRPD for ADM particle masses within $m_\chi \in [400, 4500]$ MeV and ADM mass-fractions within $F_\chi \in [0, 3]\%$. The interval on F_χ was chosen such that it extends through and beyond the ADM mass-fraction prior space defined in Sec. III C. The lower bound on the ADM particle mass interval is determined such that no ADM halo configurations are produced for neutron stars with mass $>1M_\odot$ with $F_\chi = 3\%$ and $g_\chi/m_\phi = 0$ MeV^{-1}, which ensures only ADM cores will be accounted for all $F_\chi \in [0, 3]\%$. Moreover, the upper bound of $m_\chi = 4500$ MeV is calculated by determining the largest ADM particle mass such that the maximum mass is at least $1M_\odot$ for $F_\chi = 3\%$ and $g_\chi/m_\phi = 0$ MeV^{-1}.

Adopting the upper bound of the ADM particle mass interval to be $m_\chi = 4500$ MeV captures the physically relevant ADM core configurations because our Bayesian analysis framework assigns all neutron stars with masses $<1M_\odot$ a zero likelihood evaluation.

In Fig. 7 we show the RRPD distribution between the mass-radius relations of zero self-repulsion and $g_\chi/m_\phi = 10^{-5}\ \mathrm{MeV}^{-1}$ for three representative baryonic EoSs, each of varying stiffness (top left panel), in the m_χ-F_χ plane. For each baryonic EoS, we space each ADM particle mass by $\Delta m_\chi = 250$ MeV and each mass-fraction by $\Delta F_\chi = 0.1\%$ because, when all other EoS parameters are held fixed, both Δm_χ and ΔF_χ have a small overall effect on the resulting mass-radius relation between each respective step. Although the RRPD distribution is different between each of the baryonic EoSs using Δm_χ and ΔF_χ, the maximum RRPD value is $4 \times 10^{-3}\%$ for the soft, intermediately stiff, and stiff baryonic EoSs. Therefore from this observation, we conclude that $g_\chi/m_\phi = 10^{-5}\ \mathrm{MeV}^{-1}$ is a sufficient approximation for $g_\chi/m_\phi = 0\ \mathrm{MeV}^{-1}$, regardless of the baryonic EoS, because the maximum RRPD value is $4 \times 10^{-3}\%$ which is several orders of magnitude below the observational uncertainties of neutron star radii considered in this work.

Figure 8 shows the RRPD distribution between the mass-radius relations of $g_\chi/m_\phi = 0\ \mathrm{MeV}^{-1}$ and $g_\chi/m_\phi = 10^{-5}\ \mathrm{MeV}^{-1}$ in which the step size between ADM particle mass points (Δm_χ) and ADM mass-fractions (ΔF_χ) is reduced. Note that we fix the underlying baryonic EoS to be the intermediately stiff EoS from Fig. 7. Reducing the ADM particle mass and mass-fraction step sizes will impact the overall mass-radius relation less between each successive step, thus allowing for better interpolations between grid points in the m_χ-F_χ plane. An improved interpolation between (m_χ, F_χ) grid points will allow for the dependency of the RRPD distribution on the grid spacing to be determined. Here we have reduced Δm_χ from 250 to 100 MeV (top right panel) and ΔF_χ from 0.1% to 0.05% (bottom left panel). Figure 8, shows that for both cases in which we set $\Delta m_\chi = 100$ MeV and $\Delta F_\chi = 0.05\%$, the maximum RRPD value remains below $4 \times 10^{-3}\%$. From this observation, we find that the RRPD values are insensitive to variations in Δm_χ and ΔF_χ.

Finally, based on all of the previous observations, we conclude that $g_\chi/m_\phi = 10^{-5}\ \mathrm{MeV}^{-1}$ is an adequate approximation to $0\ \mathrm{MeV}^{-1}$ within the interval of $m_\chi \in [400, 4500]$ MeV and $F_\chi \in [0, 3]\%$, regardless of the choice of Δm_χ, ΔF_χ, and baryonic EoS.

[1] K. Hebeler, J. M. Lattimer, C. J. Pethick, and A. Schwenk, Equation of state and neutron star properties constrained by nuclear physics and observation, Astrophys. J. **773**, 11 (2013).

[2] M. Oertel, M. Hempel, T. Klähn, and S. Typel, Equations of state for supernovae and compact stars, Rev. Mod. Phys. **89**, 015007 (2017).

[3] M. E. Caplan, A. S. Schneider, and C. J. Horowitz, Elasticity of nuclear pasta, Phys. Rev. Lett. **121**, 132701 (2018).

[4] L. Tolos and L. Fabbietti, Strangeness in nuclei and neutron stars, Prog. Part. Nucl. Phys. **112**, 103770 (2020).

[5] G. F. Burgio, H.-J. Schulze, I. Vidaña, and J.-B. Wei, Neutron stars and the nuclear equation of state, Prog. Part. Nucl. Phys. **120**, 103879 (2021).

[6] Ming-Zhe Han, Yong-Jia Huang, Shao-Peng Tang, and Yi-Zhong Fan, Plausible presence of new state in neutron stars with masses above 0.98MTOV, Sci. Bull. **68**, 913 (2023).

[7] J. Keller, K. Hebeler, C. J. Pethick, and A. Schwenk, Neutron star matter as a dilute solution of protons in neutrons, Phys. Rev. Lett. **132**, 232701 (2024).

[8] Lee Lindblom, Determining the nuclear equation of state from neutron-star masses and radii, Astrophys. J. **398**, 569 (1992).

[9] Anna L. Watts, Constraining the neutron star equation of state using pulse profile modeling, in *Xiamen-CUSTIPEN Workshop on the Equation of State of Dense Neutron-Rich Matter in the Era of Gravitational Wave Astronomy*, American Institute of Physics Conference Series Vol. 2127 (2019), p. 020008, 10.1063/1.5117798.

[10] Slavko Bogdanov, Frederick K. Lamb, Simin Mahmoodifar, M. Coleman Miller, Sharon M. Morsink, Thomas E. Riley, Tod E. Strohmayer, Albert K. Tung, Anna L. Watts, Alexander J. Dittmann, Deepto Chakrabarty, Sebastien Guillot, Zaven Arzoumanian, and Keith C. Gendreau, Constraining the neutron star mass-radius relation and dense matter equation of state with NICER. II. Emission from hot spots on a rapidly rotating neutron star, Astrophys. J. Lett. **887**, L26 (2019).

[11] Slavko Bogdanov, Alexander J. Dittmann, Wynn C. G. Ho, Frederick K. Lamb, Simin Mahmoodifar, M. Coleman Miller, Sharon M. Morsink, Thomas E. Riley, Tod E. Strohmayer, Anna L. Watts, Devarshi Choudhury, Sebastien Guillot, Alice K. Harding, Paul S. Ray, Zorawar Wadiasingh, Michael T. Wolff, Craig B. Markwardt, Zaven Arzoumanian, and Keith C. Gendreau, Constraining the neutron star mass-radius relation and dense matter equation of state with NICER.

III. Model description and verification of parameter estimation codes, Astrophys. J. Lett. **914**, L15 (2021).

[12] Keith C. Gendreau *et al.*, The Neutron star Interior Composition Explorer (NICER): Design and development, In *Space Telescopes and Instrumentation 2016: Ultraviolet to Gamma Ray*, edited by Jan-Willem A. den Herder, Tadayuki Takahashi, and Marshall Bautz, Society of Photo-Optical Instrumentation Engineers (SPIE) Conference Series Vol. 9905 (2016), p. 99051H, 10.1117/12.2231304.

[13] E. Fonseca *et al.*, Refined mass and geometric measurements of the high-mass PSR J0740 + 6620, Astrophys. J. Lett. **915**, L12 (2021).

[14] Thomas E. Riley *et al.*, A NICER view of the massive pulsar PSR J0740 + 6620 informed by radio timing and XMM-Newton spectroscopy, Astrophys. J. Lett. **918**, L27 (2021).

[15] M. C. Miller *et al.*, The radius of PSR J0740 + 6620 from NICER and XMM-Newton data, Astrophys. J. Lett. **918**, L28 (2021).

[16] Tuomo Salmi, Serena Vinciguerra, Devarshi Choudhury, Thomas E. Riley, Anna L. Watts, Ronald A. Remillard, Paul S. Ray, Slavko Bogdanov, Sebastien Guillot, Zaven Arzoumanian, Cecilia Chirenti, Alexander J. Dittmann, Keith C. Gendreau, Wynn C. G. Ho, M. Coleman Miller, Sharon M. Morsink, Zorawar Wadiasingh, and Michael T. Wolff, The radius of PSR J0740 + 6620 from NICER with NICER background estimates, Astrophys. J. **941**, 150 (2022).

[17] Tuomo Salmi *et al.*, The radius of the high-mass Pulsar PSR J0740 + 6620 with 3.6 yr of NICER data, Astrophys. J. **974**, 294 (2024).

[18] Alexander J. Dittmann *et al.*, A more precise measurement of the radius of PSR J0740 + 6620 using updated NICER data, Astrophys. J. **974**, 295 (2024).

[19] T. E. Riley, A. L. Watts, S. Bogdanov, P. S. Ray, R. M. Ludlam, S. Guillot, Z. Arzoumanian, C. L. Baker, A. V. Bilous, D. Chakrabarty, K. C. Gendreau, A. K. Harding, W. C. G. Ho, J. M. Lattimer, S. M. Morsink, and T. E. Strohmayer, A NICER view of PSR J0030 + 0451: Millisecond pulsar parameter estimation, Astrophys. J. Lett. **887**, L21 (2019).

[20] M. C. Miller *et al.*, PSR J0030 + 0451 mass and radius from NICER data and implications for the properties of neutron star matter, Astrophys. J. Lett. **887**, L24 (2019).

[21] Serena Vinciguerra, Tuomo Salmi, Anna L. Watts, Devarshi Choudhury, Thomas E. Riley, Paul S. Ray, Slavko Bogdanov, Yves Kini, Sebastien Guillot, Deepto Chakrabarty, Wynn C. G. Ho, Daniela Huppenkothen, Sharon M. Morsink, Zorawar Wadiasingh, and Michael T. Wolff, An updated mass-radius analysis of the 2017-2018 NICER data set of PSR J0030 + 0451, Astrophys. J. **961**, 62 (2024).

[22] Devarshi Choudhury *et al.*, A NICER view of the nearest and brightest millisecond pulsar: PSR J0437–4715, Astrophys. J. Lett. **971**, L20 (2024).

[23] Daniel J. Reardon *et al.*, The neutron star mass, distance, and inclination from precision timing of the brilliant millisecond pulsar J0437-4715, Astrophys. J. Lett. **971**, L18 (2024).

[24] Tuomo Salmi *et al.*, A NICER view of PSR J1231 − 1411: A complex case, Astrophys. J. **976**, 58 (2024).

[25] G. Raaijmakers, T. E. Riley, A. L. Watts, S. K. Greif, S. M. Morsink, K. Hebeler, A. Schwenk, T. Hinderer, S. Nissanke, S. Guillot, Z. Arzoumanian, S. Bogdanov, D. Chakrabarty, K. C. Gendreau, W. C. G. Ho, J. M. Lattimer, R. M. Ludlam, and M. T. Wolff, A Nicer view of PSR J0030 + 0451: Implications for the dense matter equation of state, Astrophys. J. Lett. **887**, L22 (2019).

[26] G. Raaijmakers, S. K. Greif, T. E. Riley, T. Hinderer, K. Hebeler, A. Schwenk, A. L. Watts, S. Nissanke, S. Guillot, J. M. Lattimer, and R. M. Ludlam, Constraining the dense matter equation of state with joint analysis of NICER and LIGO/Virgo measurements, Astrophys. J. Lett. **893**, L21 (2020).

[27] G. Raaijmakers, S. K. Greif, K. Hebeler, T. Hinderer, S. Nissanke, A. Schwenk, T. E. Riley, A. L. Watts, J. M. Lattimer, and W. C. G. Ho, Constraints on the dense matter equation of state and neutron star properties from NICER's mass-radius estimate of PSR J0740 + 6620 and multimessenger observations, Astrophys. J. Lett. **918**, L29 (2021).

[28] Jia Jie Li, Armen Sedrakian, and Mark Alford, Relativistic hybrid stars in light of the NICER PSR J0740 + 6620 radius measurement, Phys. Rev. D **104**, L121302 (2021).

[29] Isaac Legred, Katerina Chatziioannou, Reed Essick, Sophia Han, and Philippe Landry, Impact of the PSR J0740 + 6620 radius constraint on the properties of high-density matter, Phys. Rev. D **104**, 063003 (2021).

[30] Peter T. H. Pang, Ingo Tews, Michael W. Coughlin, Mattia Bulla, Chris Van Den Broeck, and Tim Dietrich, Nuclear physics multimessenger astrophysics constraints on the neutron star equation of state: Adding NICER's PSR J0740 + 6620 measurement, Astrophys. J. **922**, 14 (2021).

[31] Shao-Peng Tang, Jin-Liang Jiang, Ming-Zhe Han, Yi-Zhong Fan, and Da-Ming Wei, Constraints on the phase transition and nuclear symmetry parameters from PSR J0740 + 6620 and multimessenger data of other neutron stars, Phys. Rev. D **104**, 063032 (2021).

[32] Eemeli Annala, Tyler Gorda, Evangelia Katerini, Aleksi Kurkela, Joonas Nättilä, Vasileios Paschalidis, and Aleksi Vuorinen, Multimessenger constraints for ultradense matter, Phys. Rev. X **12**, 011058 (2022).

[33] Bhaskar Biswas, Bayesian model selection of neutron star equations of state using multi-messenger observations, Astrophys. J. **926**, 75 (2022).

[34] Nathan Rutherford, Melissa Mendes, Isak Svensson, Achim Schwenk, Anna L. Watts, Kai Hebeler, Jonas Keller, Chanda Prescod-Weinstein, Devarshi Choudhury, Geert Raaijmakers, Tuomo Salmi, Patrick Timmerman, Serena Vinciguerra, Sebastien Guillot, and James M. Lattimer, Constraining the dense matter equation of state with new NICER mass–radius measurements and new chiral effective field theory inputs, Astrophys. J. Lett. **971**, L19 (2024).

[35] Chun Huang, Geert Raaijmakers, Anna L. Watts, Laura Tolos, and Constança Providência, Constraining a relativistic mean field model using neutron star mass-radius measurements I: Nucleonic models, Mon. Not. R. Astron. Soc. **529**, 4650 (2024).

[36] J. Keller, K. Hebeler, and A. Schwenk, Nuclear equation of state for arbitrary proton fraction and temperature based on chiral effective field theory and a Gaussian process emulator, Phys. Rev. Lett. **130**, 072701 (2023).

[37] Anna L. Watts *et al.*, Dense matter with eXTP, Sci. China Phys. Mech. Astron. **62**, 29503 (2019).

[38] Paul S. Ray *et al.*, STROBE-X: X-ray timing and spectroscopy on dynamical timescales from microseconds to years, arXiv:1903.03035.

[39] Kirpal Nandra *et al.*, The hot and energetic universe: A white paper presenting the science theme motivating the Athena + mission, arXiv:1306.2307.

[40] Ann E. Nelson, Sanjay Reddy, and Dake Zhou, Dark halos around neutron stars and gravitational waves, J. Cosmol. Astropart. Phys. 07 (2019) 012.

[41] V. Sagun, E. Giangrandi, O. Ivanytskyi, I. Lopes, and K. A. Bugaev, Constraints on the fermionic dark matter from observations of neutron stars, Proc. Sci. PANIC2021 (**2022**) 313.

[42] Robin Fynn Diedrichs, Niklas Becker, Cédric Jockel, Jan-Erik Christian, Laura Sagunski, and Jürgen Schaffner-Bielich, Tidal deformability of fermion-boson stars: Neutron stars admixed with ultralight dark matter, Phys. Rev. D **108**, 064009 (2023).

[43] Joseph Bramante and Nirmal Raj, Dark matter in compact stars, Phys. Rep. **1052**, 1 (2024).

[44] Zakary Buras-Stubbs and Ilídio Lopes, Bosonic dark matter dynamics in hybrid neutron stars, Phys. Rev. D **109**, 043043 (2024).

[45] Atanu Guha and Debashree Sen, Constraining the mass of fermionic dark matter from its feeble interaction with hadronic matter via dark mediators in neutron stars, Phys. Rev. D **109**, 043038 (2024).

[46] Cédric Jockel and Laura Sagunski, Fermion Proca stars: Vector-dark-matter-admixed neutron stars, Particles **7**, 52 (2024).

[47] Shafayat Shawqi and Sharon M. Morsink, Interpreting mass and radius measurements of neutron stars with dark matter halos, Astrophys. J. **975**, 123 (2024).

[48] Zhiqiang Miao, Yaofeng Zhu, Ang Li, and Feng Huang, Dark matter admixed neutron star properties in the light of x-ray pulse profile observations, Astrophys. J. **936**, 69 (2022).

[49] Soroush Shakeri and Davood Rafiei Karkevandi, Bosonic dark matter in light of the NICER precise mass-radius measurements, Phys. Rev. D **109**, 043029 (2024).

[50] Sarah Louisa Pitz and Jürgen Schaffner-Bielich, Generating ultracompact neutron stars with bosonic dark matter, Phys. Rev. D **111**, 043050 (2025).

[51] John Ellis, Gert Hütsi, Kristjan Kannike, Luca Marzola, Martti Raidal, and Ville Vaskonen, Dark matter effects on neutron star properties, Phys. Rev. D **97**, 123007 (2018).

[52] O. Ivanytskyi, V. Sagun, and I. Lopes, Neutron stars: New constraints on asymmetric dark matter, Phys. Rev. D **102**, 063028 (2020).

[53] Ben Kain, Dark matter admixed neutron stars, Phys. Rev. D **103**, 043009 (2021).

[54] Davood Rafiei Karkevandi, Soroush Shakeri, Violetta Sagun, and Oleksii Ivanytskyi, Bosonic dark matter in neutron stars and its effect on gravitational wave signal, Phys. Rev. D **105**, 023001 (2022).

[55] Davood Rafiei Karkevandi, Mahboubeh Shahrbaf, Soroush Shakeri, and Stefan Typel, Exploring the distribution and impact of bosonic dark matter in neutron stars, Particles **7**, 201 (2024).

[56] Mar Bastero-Gil, Teresa Huertas-Roldan, and Daniel Santos, Neutron decay anomaly, neutron stars, and dark matter, Phys. Rev. D **110**, 083003 (2024).

[57] Domenico Scordino and Ignazio Bombaci, Dark matter admixed neutron stars with a realistic nuclear equation of state from chiral nuclear interactions, J. High Energy Astrophys. **45**, 371 (2025).

[58] Andreas Konstantinou, The effect of a dark matter core on the structure of a rotating neutron star, Astrophys. J. **968**, 83 (2024).

[59] H. C. Das, Ankit Kumar, Bharat Kumar, and Suresh Kumar Patra, Dark matter effects on the compact star properties, Galaxies **10**, 14 (2022).

[60] Arpan Das, Tuhin Malik, and Alekha C. Nayak, Dark matter admixed neutron star properties in light of gravitational wave observations: A two fluid approach, Phys. Rev. D **105**, 123034 (2022).

[61] Debashree Sen and Atanu Guha, Implications of feebly interacting dark sector on neutron star properties and constraints from GW170817, Mon. Not. R. Astron. Soc. **504**, 3354 (2021).

[62] Atanu Guha and Debashree Sen, Feeble DM-SM interaction via new scalar and vector mediators in rotating neutron stars, J. Cosmol. Astropart. Phys. 09 (2021) 027.

[63] Edoardo Giangrandi, Violetta Sagun, Oleksii Ivanytskyi, Constança Providência, and Tim Dietrich, The effects of self-interacting bosonic dark matter on neutron star properties, Astrophys. J. **953**, 115 (2023).

[64] Mikel F. Barbat, Jürgen Schaffner-Bielich, and Laura Tolos, Comprehensive study of compact stars with dark matter, Phys. Rev. D **110**, 023013 (2024).

[65] Hongyi Sun and Dehua Wen, New criterion for the existence of dark matter in neutron stars, Phys. Rev. D **109**, 123037 (2024).

[66] Prashant Thakur, Tuhin Malik, and Tarun Kumar Jha, Towards uncovering dark matter effects on neutron star properties: A machine learning approach, Particles **7**, 80 (2024).

[67] Prashant Thakur, Tuhin Malik, Arpan Das, T. K. Jha, and Constança Providência, Exploring robust correlations between fermionic dark matter model parameters and neutron star properties: A two-fluid perspective, Phys. Rev. D **109**, 043030 (2024).

[68] Swarnim Shirke, Bikram Keshari Pradhan, Debarati Chatterjee, Laura Sagunski, and Jürgen Schaffner-Bielich, Effects of dark matter on f-mode oscillations of neutron stars, Phys. Rev. D **110**, 063025 (2024).

[69] Pratik Thakur, Anil Kumar, Vivek Baruah Thapa, Vishal Parmar, and Monika Sinha, Exploring non-radial oscillation modes in dark matter admixed neutron stars, J. Cosmol. Astropart. Phys. 12 (2024) 042.

[70] Suman Pal and Gargi Chaudhuri, Effect of dark matter interaction on hybrid star in the light of the recent

astrophysical observations, J. Cosmol. Astropart. Phys. 10 (2024) 064.

[71] Mauro Mariani, Conrado Albertus, M. del Rosario Alessandroni, Milva G. Orsaria, M. Ángeles Pérez-García, and Ignacio F. Ranea-Sandoval, Constraining self-interacting fermionic dark matter in admixed neutron stars using multimessenger astronomy, Mon. Not. R. Astron. Soc. **527**, 6795 (2024).

[72] Premachand Mahapatra, Chiranjeeb Singha, Ayush Hazarika, and Prasanta Kumar Das, Implications of fermionic dark matter interactions on anisotropic neutron stars, arXiv:2408.14020.

[73] Ankit Kumar and Hajime Sotani, Constraints on the parameter space in dark matter admixed neutron stars, Phys. Rev. D **110**, 063001 (2024).

[74] Pinku Routaray, Sailesh Ranjan Mohanty, H. C. Das, Sayantan Ghosh, P. J. Kalita, Vishal Parmar, and Bharat Kumar, Investigating dark matter-admixed neutron stars with NITR equation of state in light of PSR J0952-0607, J. Cosmol. Astropart. Phys. 10 (2023) 073.

[75] M. Iu. Khlopov, B. A. Malomed, and Ia. B. Zeldovich, Gravitational instability of scalar fields and formation of primordial black holes, Mon. Not. R. Astron. Soc. **215**, 575 (1985).

[76] Gianfranco Bertone and Malcolm Fairbairn, Compact stars as dark matter probes, Phys. Rev. D **77**, 043515 (2008).

[77] Chris Kouvaris and Peter Tinyakov, Constraining asymmetric dark matter through observations of compact stars, Phys. Rev. D **83**, 083512 (2011).

[78] Moira I. Gresham and Kathryn M. Zurek, Asymmetric dark stars and neutron star stability, Phys. Rev. D **99**, 083008 (2019).

[79] Andreas Bauswein, Gang Guo, Jr. Lien-Hua, Yen-Hsun Lin, and Meng-Ru Wu, Compact dark objects in neutron star mergers, Phys. Rev. D **107**, 083002 (2023).

[80] Hannes R. Rüter, Violetta Sagun, Wolfgang Tichy, and Tim Dietrich, Quasiequilibrium configurations of binary systems of dark matter admixed neutron stars, Phys. Rev. D **108**, 124080 (2023).

[81] Mattia Emma, Federico Schianchi, Francesco Pannarale, Violetta Sagun, and Tim Dietrich, Numerical simulations of dark matter admixed neutron star binaries, Particles **5**, 273 (2022).

[82] Rebecca K. Leane and Joshua Tong, Optimal celestial bodies for dark matter detection, J. Cosmol. Astropart. Phys. 12 (2024) 031.

[83] Nathan Rutherford, Geert Raaijmakers, Chanda Prescod-Weinstein, and Anna Watts, Constraining bosonic asymmetric dark matter with neutron star mass-radius measurements, Phys. Rev. D **107**, 103051 (2023).

[84] Kalliopi Petraki and Raymond R. Volkas, Review of asymmetric dark matter, Int. J. Mod. Phys. A **28**, 1330028 (2013).

[85] Kalliopi Petraki, Lauren Pearce, and Alexander Kusenko, Self-interacting asymmetric dark matter coupled to a light massive dark photon, J. Cosmol. Astropart. Phys. 07 (2014) 039.

[86] Sharon M. Morsink, Denis A. Leahy, Coire Cadeau, and John Braga, The Oblate Schwarzschild approximation for light curves of rapidly rotating neutron stars, Astrophys. J. **663**, 1244 (2007).

[87] Mohammad AlGendy and Sharon M. Morsink, Universality of the acceleration due to gravity on the surface of a rapidly rotating neutron star, Astrophys. J. **791**, 78 (2014).

[88] P. S. Ray *et al.*, STROBE-X: A probe-class mission for x-ray spectroscopy and timing on timescales from microseconds to years, In *Space Telescopes and Instrumentation 2018: Ultraviolet to Gamma Ray*, Society of Photo-Optical Instrumentation Engineers (SPIE) Conference Series Vol. 10699 (2018), p. 1069919, 10.1117/12.2312257.

[89] Richard C. Tolman, Static solutions of Einstein's field equations for spheres of fluid, Phys. Rev. **55**, 364 (1939).

[90] J. R. Oppenheimer and G. M. Volkoff, On massive neutron cores, Phys. Rev. **55**, 374 (1939).

[91] Violetta Sagun, Edoardo Giangrandi, Tim Dietrich, Oleksii Ivanytskyi, Rodrigo Negreiros, and Constança Providência, What is the nature of the HESS J1731-347 compact object?, Astrophys. J. **958**, 49 (2023).

[92] Fredrik Sandin and Paolo Ciarcelluti, Effects of mirror dark matter on neutron stars, Astropart. Phys. **32**, 278 (2009).

[93] Teresa Marrodán Undagoitia and Ludwig Rauch, Dark matter direct-detection experiments, J. Phys. G Nucl. Phys. **43**, 013001 (2016).

[94] Ermal Rrapaj and Sanjay Reddy, Nucleon-nucleon bremsstrahlung of dark gauge bosons and revised supernova constraints, Phys. Rev. C **94**, 045805 (2016).

[95] Fazlollah Hajkarim, Jürgen Schaffner-Bielich, and Laura Tolos, Thermodynamic consistent description of compact stars of two interacting fluids: The case of neutron stars with Higgs portal dark matter, arXiv:2412.04585.

[96] Michael Collier, Djuna Croon, and Rebecca K. Leane, Tidal Love numbers of novel and admixed celestial objects, Phys. Rev. D **106**, 123027 (2022).

[97] S. K. Greif, G. Raaijmakers, K. Hebeler, A. Schwenk, and A. L. Watts, Equation of state sensitivities when inferring neutron star and dense matter properties, Mon. Not. R. Astron. Soc. **485**, 5363 (2019).

[98] Jocelyn S. Read, Benjamin D. Lackey, Benjamin J. Owen, and John L. Friedman, Constraints on a phenomenologically parametrized neutron-star equation of state, Phys. Rev. D **79**, 124032 (2009).

[99] Gordon Baym, Christopher Pethick, and Peter Sutherland, The ground state of matter at high densities: Equation of state and stellar models, Astrophys. J. **170**, 299 (1971).

[100] C. Drischler, J. W. Holt, and C. Wellenhofer, Chiral effective field theory and the high-density nuclear equation of state, Annu. Rev. Nucl. Part. Sci. **71**, 403 (2021).

[101] I. Tews, J. Carlson, S. Gandolfi, and S. Reddy, Constraining the speed of sound inside neutron stars with chiral effective field theory interactions and observations, Astrophys. J. **860**, 149 (2018).

[102] K. Hebeler and A. Schwenk, Chiral three-nucleon forces and neutron matter, Phys. Rev. C **82**, 014314 (2010).

[103] Geert Raaijmakers, Nathan Rutherford, Patrick Timmerman, Tuomo Salmi, Anna L. Watts, Chanda Prescod-Weinstein, Isak Svensson, and Melissa Mendes, NEoST: A Python package for nested sampling of the neutron star equation of state, J. Open Source Software **10**, 6003 (2025).

[104] N. Rutherford, C. Prescod-Weinstein, and A. L. Watts, Probing fermionic asymmetric dark matter cores using

global neutron star properties: Prior and posterior samples and scripts for generating plots, Zenodo (2025), 10.5281/zenodo.15237252.

[105] Chris Kouvaris and Peter Tinyakov, Excluding light asymmetric bosonic dark matter, Phys. Rev. Lett. **107**, 091301 (2011).

[106] Wasif Husain and Anthony W. Thomas, Novel neutron decay mode inside neutron stars, J. Phys. G Nucl. Phys. **50**, 015202 (2023).

[107] Julio F. Navarro, Carlos S. Frenk, and Simon D. M. White, The structure of cold dark matter halos, Astrophys. J. **462**, 563 (1996).

[108] Hai-Nan Lin and Xin Li, The dark matter profiles in the Milky Way, Mon. Not. R. Astron. Soc. **487**, 5679 (2019).

[109] Yoshiaki Sofue, Rotation curve and mass distribution in the galactic center—from black hole to entire galaxy, Publ. Astron. Soc. Jpn. **65**, 118 (2013).

[110] K. Strobel, Ch. Schaab, and M. K. Weigel, Properties of non-rotating and rapidly rotating protoneutron stars, Astron. Astrophys. **350**, 497 (1999), arXiv:astro-ph/9908132.

[111] David Radice, Adam Burrows, David Vartanyan, M. Aaron Skinner, and Joshua C. Dolence, Electron-capture and Low-mass Iron-core-collapse Supernovae: New neutrino-radiation-hydrodynamics simulations, Astrophys. J. **850**, 43 (2017).

[112] Yudai Suwa, Takashi Yoshida, Masaru Shibata, Hideyuki Umeda, and Koh Takahashi, On the minimum mass of neutron stars, Mon. Not. R. Astron. Soc. **481**, 3305 (2018).

[113] Victor Doroshenko, Valery Suleimanov, Gerd Pühlhofer, and Andrea Santangelo, A strangely light neutron star within a supernova remnant, Nat. Astron. **6**, 1444 (2022).

[114] J. A. J. Alford and J. P. Halpern, Do central compact objects have carbon atmospheres?, Astrophys. J. **944**, 36 (2023).

[115] Afonso Ávila, Edoardo Giangrandi, Violetta Sagun, Oleksii Ivanytskyi, and Constança Providência, Rapid neutron star cooling triggered by dark matter, Mon. Not. R. Astron. Soc. **528**, 6319 (2024).

[116] Edoardo Giangrandi, Afonso Ávila, Violetta Sagun, Oleksii Ivanytskyi, and Constança Providência, The impact of asymmetric dark matter on the thermal evolution of nucleonic and hyperonic compact stars, Particles **7**, 179 (2024).

[117] Wasif Husain and Anthony W. Thomas, Possible nature of dark matter, J. Cosmol. Astropart. Phys. 10 (2021) 086.

[118] T. E. Oliphant, Python for scientific computing, Comput. Sci. Eng. **9**, 10 (2007).

[119] Brian Gough, *GNU Scientific Library Reference Manual—Third Edition* (Network Theory Ltd., 2009), ISBN 0954612078, 9780954612078.

[120] S. van der Walt, S. C. Colbert, and G. Varoquaux, The NumPy array: A structure for efficient numerical computation, Comput. Sci. Eng. **13**, 22 (2011).

[121] S. Behnel, R. Bradshaw, C. Citro, L. Dalcin, D. S. Seljebotn, and K. Smith, Cython: The best of both worlds, Comput. Sci. Eng. **13**, 31 (2011).

[122] Pauli Virtanen *et al.* (SciPy 1.0 Contributors), SciPy 1.0: Fundamental algorithms for scientific computing in Python, Nat. Methods **17**, 261 (2020).

[123] Lisandro Dalcín, Rodrigo Paz, Mario Storti, and Jorge D'Elía, MPI for Python: Performance improvements and MPI-2 extensions, J. Parallel Distrib. Comput. **68**, 655 (2008).

[124] John D. Hunter, Matplotlib: A 2D graphics environment, Comput. Sci. Eng. **9**, 90 (2007).

[125] Thomas Kluyver, Benjamin Ragan-Kelley, Fernando Pérez, Brian Granger, Matthias Bussonnier, Jonathan Frederic, Kyle Kelley, Jessica Hamrick, Jason Grout, Sylvain Corlay, Paul Ivanov, Damián Avila, Safia Abdalla, and Carol Willing, Jupyter notebooks—a publishing format for reproducible computational workflows, in *Positioning and Power in Academic Publishing: Players, Agents and Agendas*, edited by F. Loizides and B. Schmidt (IOS Press, Amsterdam, NL, 2016), pp. 87–90.

[126] F. Feroz, M. P. Hobson, E. Cameron, and A. N. Pettitt, Importance nested sampling and the MultiNest algorithm, Open J. Astrophys.**2**, 10 (2019).

[127] J. Buchner, A. Georgakakis, K. Nandra, L. Hsu, C. Rangel, M. Brightman, A. Merloni, M. Salvato, J. Donley, and D. Kocevski, X-ray spectral modelling of the AGN obscuring region in the CDFS: Bayesian model selection and catalogue, Astron. Astrophys. **564**, A125 (2014).

[128] Luke Zoltan Kelley, KALEPY: A Python package for kernel density estimation sampling and plotting, J. Open Source Software **6**, 2784 (2021).

[129] Daniel Foreman-Mackey, CORNER.py: Scatterplot matrices in Python, J. Open Source Software **1**, 24 (2016).

[130] Michael L. Waskom, SEABORN: Statistical data visualization, J. Open Source Software **6**, 3021 (2021).